MetalWalls: Simulating electrochemical interfaces between polarizable electrolytes and metallic electrodes

Alessandro Coretti, Camille Bacon, Roxanne Berthin, Alessandra Serva, Laura Scalfi, Iurii Chubak, Kateryna Goloviznina, Matthieu Haefele, Abel Marin-Laflèche, Benjamin Rotenberg, et al.

▶ To cite this version:

Alessandro Coretti, Camille Bacon, Roxanne Berthin, Alessandra Serva, Laura Scalfi, et al.. MetalWalls: Simulating electrochemical interfaces between polarizable electrolytes and metallic electrodes. Journal of Chemical Physics, 2022, 157 (18), pp.184801. 10.1063/5.0101777 . hal-03843736

HAL Id: hal-03843736

https://hal.sorbonne-universite.fr/hal-03843736

Submitted on 8 Nov 2022

HAL is a multi-disciplinary open access archive for the deposit and dissemination of scientific research documents, whether they are published or not. The documents may come from teaching and research institutions in France or abroad, or from public or private research centers.

L'archive ouverte pluridisciplinaire **HAL**, est destinée au dépôt et à la diffusion de documents scientifiques de niveau recherche, publiés ou non, émanant des établissements d'enseignement et de recherche français ou étrangers, des laboratoires publics ou privés.

Accepted to J. Chem. Phys. 10.1063/5.0101777

MetalWalls: Simulating electrochemical interfaces between polarizable electrolytes and metallic electrodes

Alessandro Coretti,[1,2,3] Camille Bacon,[4,5] Roxanne Berthin,[4,5] Alessandra Serva,[4,5] Laura Scalfi,[4,5] Iurii Chubak,[4,5] Kateryna Goloviznina,[4,5] Matthieu Haefele,[6] Abel Marin-Laflèche,[7] Benjamin Rotenberg,[4,5] Sara Bonella,[3] and Mathieu Salanne[4,5,8,a)]

[1)] *Faculty of Physics, University of Vienna, Kolingasse 14-16, 1090 Vienna, Austria*
[2)] *Department of Mathematical Sciences, Politecnico di Torino, I-10129 Torino, Italy*
[3)] *Centre Européen de Calcul Atomique et Moléculaire (CECAM), Ecole Polytechnique Fédérale de Lausanne, 1015 Lausanne, Switzerland*
[4)] *Sorbonne Université, CNRS, Physicochimie des Électrolytes et Nanosystèmes Interfaciaux, F-75005 Paris, France*
[5)] *Réseau sur le Stockage Electrochimique de l'Energie (RS2E), FR CNRS 3459, 80039 Amiens Cedex, France*
[6)] *CNRS, Université de Pau et des Pays de l'Adour, E2S UPPA, LMAP, 64000 Pau, France*
[7)] *Université Paris-Saclay, UVSQ, CNRS, CEA, Maison de la Simulation, 91191, Gif-sur-Yvette, France*
[8)] *Institut Universitaire de France (IUF), 75231 Paris, France*

(Dated: 20 July 2022)

Electrochemistry is central to many applications, ranging from biology to energy science. Studies now involve a wide range of techniques, both experimental and theoretical. Modelling and simulations methods, such as density functional theory or molecular dynamics, provide key information on the structural and dynamic properties of the systems. Of particular importance are polarization effects the electrode/electrolyte interface, which are difficult to simulate accurately. Here we show how these electrostatic interactions are taken into account in the framework of the Ewald summation method. We discuss, in particular, the formal set up for calculations that enforce periodic boundary conditions in two directions, a geometry that more closely reflects the characteristics of typical electrolyte/electrode systems and presents some differences with respect to the more common case of periodic boundary conditions in three dimensions. These formal developments are implemented and tested in MetalWalls, a molecular dynamics software which captures the polarization of the electrolyte and allows the simulation of electrodes maintained at a constant potential. We also discuss the technical aspects involved in the calculation of two sets of coupled degrees of freedom, namely the induced dipoles and the electrode charges. We validate the implementation, first on simple systems, then on the well-known interface between graphite electrodes and a room-temperature ionic liquid. We finally illustrate the capabilities of MetalWalls by studying the adsorption of a complex functionalized electrolyte on a graphite electrode.

I. INTRODUCTION

The simulation of electrochemical systems has become an important topic in chemical physics. This is mainly driven by the need for understanding the molecular mechanisms at play in devices such as batteries,[1] electrocatalysts,[2–5] supercapacitors,[6] etc. Such simulations concern bulk electrode materials[7] and electrolytes,[8] whose properties need to be well characterized and rationalized, but more and more efforts are devoted to the description of electrode/electrolyte interfaces.[9] Until recently, very little was known of the latter at the molecular scale and the only available picture was provided by theories such as the Gouy-Chapman-Stern one.[6] However, these theories are limited to simple systems,[10] and the use of concentrated electrolytes (*e.g.* ionic liquids) and complex electrode materials in current electrochemical devices requires much more sophisticated techniques, among which molecular dynamics (MD) simulation is the most widespread. Depending on the target properties, the flavor of the MD can be adapted: Classical MD, in which the forces are derived from an analytical interaction potential, is preferred when the objective is to obtain the structural, thermodynamic and transport properties of chemically inert systems, while *ab initio* MD, based on electronic structure calculations, most often in the framework of Density Functional Theory, for the evaluation of the interactions, is more adapted for studying systems undergoing chemical reactions such as chemisorption.[11]

Among the various methods used to simulate electrochemical interfaces,[9] one of the most popular was introduced by Siepmann and Sprik.[12] It consists in representing the electrode atoms using Gaussian charges, whose magnitude fluctuates in order to satisfy a constant potential condition within a given electrode, while the charge distribution within the electrolyte is represented

---

[a)] Electronic mail: mathieu.salanne@sorbonne-universite.fr

The Journal of Chemical Physics ACCEPTED MANUSCRIPT

using point charges. A difficulty when studying interfaces in MD is the handling of periodic boundary conditions (PBCs), in particular for long-ranged interactions. Usual implementations in MD codes correspond to 3D PBCs, so that interfacial systems become an infinite collection of slabs. This effect can be canceled using corrections such as the one introduced by Yeh and Berkowitz,[13] and introducing a wide layer of vacuum between periodic images.[14] Another approach is to derive explicitly the equations for 2D-periodic systems. Reed and Madden have thus formulated Ewald-type expressions for electrochemical systems made of point charge electrolytes and Gaussian charge electrodes.[15] Their equations were later corrected by Gingrich and Wilson.[16] This constant potential method was first implemented with 3D PBCs in the popular MD code LAMMPS,[17,18] and technical improvements were recently proposed to improve the efficiency of the simulations, such as the use of particle-particle-particle-mesh solver approach[19] or the use of a doubled cell approach.[20]

However, the inclusion of polarization effects often improves the accuracy of the description of liquid electrolytes.[8] In particular the dynamic properties of concentrated electrolytes, such as the diffusion coefficients, are better reproduced when including polarization.[21–23] The charge-dipole and dipole-dipole interactions are also long-ranged, so one needs to treat them appropriately.[24,25] In the presence of electrodes with Gaussian charges, the only derivation available was proposed by Pounds in his PhD thesis.[26] A second difficulty lies in the self-consistent calculation of the electrode charges and of the induced dipoles for a given configuration of the electrolyte. In general, the two problems are solved by using conjugate gradient minimization techniques (even though in the case of electrode atoms, their position is often fixed which allows the use of more efficient methods such as matrix inversion or mass-zero constrained dynamics,[27,28] but now the two problems are coupled: the charges depend on the dipoles and *vice versa*. In a first attempt to include both effects in simulations, we have used a recursive approach in which the two minimizations are performed one after each other until the two problems are converged.[29,30] However, this increases considerably the computational time, limiting the ability to simulate large systems so that only molten salts could be studied. Borodin and co-workers proposed to update the electrode charges much less frequently than the atomic positions (typically every 250 fs),[31] but they did not discuss the use of appropriate multiple time step techniques[32,33] to achieve this.

MetalWalls is a MD software dedicated to the simulation of electrochemical interfaces.[34] Here we introduce the recent implementations allowing for the inclusion of the interactions between polarizable electrolytes and metallic electrodes that are represented with fluctuating Gaussian charges. In the first section, we provide the derivation of the energies associated with these interactions within a 2D-Ewald framework. The second section discusses the optimization problem, for which we show that Jacobi preconditioning allows an efficient use of the conjugate gradient method. The implementation is then validated by simulating simple systems for which we can obtain reference results. Finally, we provide some results for two electrochemical systems. Firstly, we simulate a typical ionic liquid (1-ethyl-3-methylimidazolium bis(trifluoromethylsulfonyl)imide, EMIM-TFSI) between graphite electrodes, a system for which accurate non-polarizable force fields are available for comparison. Secondly, we study the adsorption of redox-functionalized ionic species, again on graphite, using a polarizable interaction potential recently parameterized in our group.[35]

II. INTERACTION MODEL

The model implemented in MetalWalls includes different electrostatic components. The electrolyte is modeled as a set of N_p point charges and N_d point dipoles at positions $\{\boldsymbol{r}_i\}_{i=1}^{N_p}$ and $\{\boldsymbol{r}_J\}_{J=1}^{N_d}$, respectively. Denoting by $\delta^3(\boldsymbol{r}-\boldsymbol{r}_i)$ the three-dimensional Dirac's delta centered at the point $\boldsymbol{r}_i$, the charge distribution of a point charge is simply given by

$$\varrho_i^q(\boldsymbol{r}) = q_i\delta^3(\boldsymbol{r}-\boldsymbol{r}_i) \tag{1}$$

so that, given the definition of the electric potential

$$V(\boldsymbol{r}) = \int_{\mathbb{R}^3} \mathrm{d}^3r' \, \frac{\varrho(\boldsymbol{r}')}{|\boldsymbol{r}-\boldsymbol{r}'|} \tag{2}$$

the set of point charges generates a potential in space given by

$$V^q(\boldsymbol{r}) = \sum_{i=1}^{N_p} \frac{q_i}{|\boldsymbol{r}-\boldsymbol{r}_i|} \tag{3}$$

Dipoles can be modeled as two opposite point charges connected by a rigid rod of length $\boldsymbol{\delta}$, so that the charge distribution can be written as

$$\varrho_J^{\boldsymbol{\mu}}(\boldsymbol{r}) = -q_J\delta^3(\boldsymbol{r}-\boldsymbol{r}_J+\boldsymbol{\delta}/2) + q_J\delta^3(\boldsymbol{r}-\boldsymbol{r}_J-\boldsymbol{\delta}/2) \tag{4}$$

Using again Eq. (2) and taking the limit of $\boldsymbol{\delta}\to 0$ (point-dipole approximation), the potential generated by the set of point dipoles is given by

$$V^{\boldsymbol{\mu}}(\boldsymbol{r}) = \sum_{J=1}^{N_d} \frac{\boldsymbol{\mu}_J\cdot(\boldsymbol{r}-\boldsymbol{r}_J)}{|\boldsymbol{r}-\boldsymbol{r}_J|^3} \tag{5}$$

where $\boldsymbol{\mu}_J$ is the point dipole associated to the particle J.

Electrodes are modeled using the so-called fluctuating charge model[12], which considers the metallic electrodes composed by N_g Gaussian-distributed charges

$$\varrho_\alpha^Q(\boldsymbol{r}) = Q_\alpha\left(\frac{\eta_\alpha^2}{\pi}\right)^{\frac{3}{2}} \exp\left[-\eta_\alpha^2(\boldsymbol{r}-\boldsymbol{R}_\alpha)^2\right] \tag{6}$$

The Journal of Chemical Physics ACCEPTED MANUSCRIPT
This is the author's peer reviewed, accepted manuscript. However, the online version of record will be different from this version once it has been copyedited and typeset.
PLEASE CITE THIS ARTICLE AS DOI:10.1063/5.0101777
AIP Publishing

placed at fixed sites $\{\boldsymbol{R}_\alpha\}_{\alpha=1}^{N_g}$, with η_α being a model parameter (which can be changed to tune the electrode metallicity[36]). The potential generated by this set of charges is given by

$$V^Q(\boldsymbol{r}) = \sum_{\alpha=1}^{N_g} \frac{Q_\alpha}{|\boldsymbol{r}-\boldsymbol{R}_\alpha|}\,\mathrm{erf}(\eta_\alpha|\boldsymbol{r}-\boldsymbol{R}_\alpha|) \tag{7}$$

The interaction energy for a system of Gaussian-distributed charges, point charges and point dipoles is composed by the six contributions

$$U_{\mathrm{elec}} = U^{\boldsymbol{\mu}\boldsymbol{\mu}} + U^{QQ} + U^{qq} + 2U^{Q\boldsymbol{\mu}} + 2U^{Qq} + 2U^{q\boldsymbol{\mu}} \tag{8}$$

where the superscripts indicate the specific interactions, so, for example, $U^{q\boldsymbol{\mu}}$ is the interaction between the electrolyte's point charges and the point dipoles. These energies are derived from the charge distribution density and from the electrostatic potential of the particular electrostatic components involved through the relation

$$U_{\mathrm{elec}} = \frac{1}{2}\int_{\mathbb{R}^3\times\mathbb{R}^3} \mathrm{d}^3r\mathrm{d}^3r'\,\frac{\varrho(\boldsymbol{r})\varrho(\boldsymbol{r}')}{|\boldsymbol{r}-\boldsymbol{r}'|} = \frac{1}{2}\int_{\mathbb{R}^3} \mathrm{d}^3r\,\varrho(\boldsymbol{r})V(\boldsymbol{r}) \tag{9}$$

where in going from the second to the third equality, the definition of the electrostatic potential given in Eq. (2) has been recognized. In what follows we explicitly report the expressions for the 2D Ewald decomposition for all the energy terms appearing in Eq. (8). Some of these terms are already reported in the literature (see for example Ref. 15 for U^{qq}, U^{QQ} and U^{Qq}) and others are only discussed in the case of 3D PBC ($U^{\boldsymbol{\mu}\boldsymbol{\mu}}$ and $U^{q\boldsymbol{\mu}}$ in Ref. 37). To the authors knowledge, no derivation or Ewald decomposition has ever been reported in the literature for the term $U^{Q\boldsymbol{\mu}}$. We report a complete derivation for energies and forces for this term in the Supplementary Material.

A. 2D-PBC Ewald decomposition for Energies

Here we summarize the Ewald decomposition in the case of 2D-PBC for all the energy terms involved in the model of a system of interacting point-charges, point-dipoles and Gaussian charges. This is relevant because, in electrochemical systems, PBC are usually enforced only in the directions parallel to the electrodes. Assuming the electrodes extending on the xy-plane, the presence of replicated simulation boxes means that, for every particle in the system, there are an infinite number of other replicas at relative positions $\boldsymbol{m} = (n_xL_x, n_yL_y, n_zL_z)$ where $\boldsymbol{L} = (L_x, L_y, L_z)$ are the dimensions of the primary simulation box and, in the chosen geometry, $n_x, n_y \in \mathbb{Z}$ while $n_z = 0$. To compute the energy of the system, a sum over all the replicas (i.e., over all boxes) needs to be performed. This sum will be noted in what follows by $\sum_{\boldsymbol{n}}$ and it runs over all the integers from $-\infty$ to $+\infty$ in all the components involved in the PBC. As commonly done in the Ewald decomposition, the conditional convergence of the Coulomb interaction is solved for each term of Eq. (8) by dividing the infinite summation over periodic boxes in a short-range part in real space (denoted by U_{sr}) and a long-range in reciprocal space (denoted by U_{lr}). Eventual artifacts arising from overcounting are taken into account through a self-energy term (denoted by U_{self}). The reciprocal space is characterized by the wavevectors indexes $\boldsymbol{k} \in \mathbb{Z}^3$. The size of the system defines the reciprocal space wavevectors through the relation $\boldsymbol{h} = (2\pi k_x/L_x, 2\pi k_y/L_y, 2\pi k_z/L_z)$, where, once again in the chosen geometry, $k_x, k_y \in \mathbb{Z}$ and $k_z = 0$. Due to the 2D PBC, the long-range term is to be divided in turn in the contribution from $\boldsymbol{k} = 0$ and $\boldsymbol{k} \neq 0$, which are denoted by $U_{\mathrm{lr},0}$ and $U_{\mathrm{lr},*}$, respectively. In the following we assume the periodic part of the system to be embedded in a medium with infinite dielectric constant (the so-called "tinfoil boundary conditions"[38]) together with global electroneutrality of the system.

The Journal of Chemical Physics ACCEPTED MANUSCRIPT
AIP Publishing
This is the author's peer reviewed, accepted manuscript. However, the online version of record will be different from this version once it has been copyedited and typeset.
PLEASE CITE THIS ARTICLE AS DOI:10.1063/5.0101777

1. Point charge-point charge interaction: U^{qq}

The expression is written as a sum of four terms $U^{qq} = U^{qq}_{\rm sr} + U^{qq}_{\rm lr,0} + U^{qq}_{\rm lr,*} + U^{qq}_{\rm self}$,

$$U^{qq}_{\rm sr} = \frac{1}{2}\sum_{i=1}^{N_p}\sum_{j=1}^{N_p}\sum_{\boldsymbol{n}}{}' \frac{q_i q_j}{|\boldsymbol{r}_{ij}+\boldsymbol{m}|}\operatorname{erfc}\big[\alpha|\boldsymbol{r}_{ij}+\boldsymbol{m}|\big] \tag{10a}$$

$$U^{qq}_{\rm lr,0} = -\frac{\sqrt{\pi}}{L_x L_y}\sum_{i=1}^{N_p}\sum_{j=1}^{N_p} q_i q_j \left(\frac{\exp\big[-\alpha^2 z_{ij}^2\big]}{\alpha} + \sqrt{\pi} z_{ij}\operatorname{erf}\big[\alpha z_{ij}\big]\right) \tag{10b}$$

$$U^{qq}_{\rm lr,*} = \frac{1}{L_x L_y}\sum_{i=1}^{N_p}\sum_{j=1}^{N_p}\int_{-\infty}^{\infty} \mathrm{d}u \sum_{\boldsymbol{k}\neq 0} q_i q_j \frac{\exp\Big[-\frac{h^2+u^2}{4\alpha^2}\Big]}{h^2+u^2}\exp\Big[\mathrm{i}\big(\boldsymbol{h}\cdot\boldsymbol{r}_{ij} + u z_{ij}\big)\Big] \tag{10c}$$

$$U^{qq}_{\rm self} = -\frac{\alpha}{\sqrt{\pi}}\sum_{i=1}^{N_p} q_i^2 \tag{10d}$$

In Eq. (10a) we have introduced the primed sum over the replicated boxes to indicate that for $\boldsymbol{n} = (0,0,0)$ the case $i = j$ is excluded. With some differences in notation these terms have already been reported in Ref. 15.

2. Point charge-Gaussian charge interaction: U^{qQ}

No self interaction has to be considered in this case as particles are of different nature. This fact is also highlighted by the extended notation $\boldsymbol{r}_i - \boldsymbol{R}_\alpha$ in place of the corresponding $\boldsymbol{r}_{ij}$ of the previous set. We can then write $U^{qQ} = U^{qQ}_{\rm sr} + U^{qQ}_{\rm lr,0} + U^{qQ}_{\rm lr,*}$, with the following expressions for the various terms:

$$U^{qQ}_{\rm sr} = \frac{1}{2}\sum_{i=1}^{N_p}\sum_{\alpha=1}^{N_g}\sum_{\boldsymbol{n}} \frac{q_i Q_\alpha}{|\boldsymbol{r}_i-\boldsymbol{R}_\alpha+\boldsymbol{m}|}\Big(\operatorname{erfc}\big[\alpha(|\boldsymbol{r}_i-\boldsymbol{R}_\alpha+\boldsymbol{m}|)\big] - \operatorname{erfc}\big[\eta_\alpha(|\boldsymbol{r}_i-\boldsymbol{R}_\alpha+\boldsymbol{m}|)\big]\Big) \tag{11a}$$

$$U^{qQ}_{\rm lr,0} = -\frac{\sqrt{\pi}}{L_x L_y}\sum_{i=1}^{N_p}\sum_{\alpha=1}^{N_g} q_i Q_\alpha \left(\frac{\exp\big[-\alpha^2(z_i-Z_\alpha)^2\big]}{\alpha} + \sqrt{\pi}(z_i-Z_\alpha)\operatorname{erf}\big[\alpha(z_i-Z_\alpha)\big]\right) \tag{11b}$$

$$U^{qQ}_{\rm lr,*} = \frac{1}{L_x L_y}\sum_{\alpha=1}^{N_g}\sum_{i=1}^{N_p}\int_{-\infty}^{\infty} \mathrm{d}u \sum_{\boldsymbol{k}\neq 0} Q_\alpha q_i \frac{\exp\Big[-\frac{h^2+u^2}{4\alpha^2}\Big]}{h^2+u^2}\exp\Big[\mathrm{i}\big(\boldsymbol{h}\cdot(\boldsymbol{R}_\alpha-\boldsymbol{r}_i) + u(Z_\alpha - z_i)\big)\Big] \tag{11c}$$

$$\tag{11d}$$

Note also that long-range interactions have the same form as in the case of the point-charge to point-charge case, with the integrated Gaussian charge Q_α in place of the point charge q_i. Also these terms were defined in Ref. 15 with some differences in notation.

3. Point charge-point dipole interaction: $U^{q\mu}$

The interaction energy between point charges and point dipoles has been previously computed, for example, in Ref. 24 where 3D PBC are assumed. The extension to the 2D PBC case does not present particular difficulties and we report it in what follows. Note that, once again, particles involved in the sums belong to different set. Even though they both refer to electrolyte particles, we could imagine to have point-charge particles which are non-polarizable and also the opposite situation is possible. To emphasize this aspect we use the extended notation $\boldsymbol{r}_i - \boldsymbol{r}_J$ in place of $\boldsymbol{r}_{ij}$ also in this case. For the same reason, no self-interaction term is present and the interaction energy can be split as

The Journal of Chemical Physics ACCEPTED MANUSCRIPT

This is the author's peer reviewed, accepted manuscript. However, the online version of record will be different from this version once it has been copyedited and typeset.
PLEASE CITE THIS ARTICLE AS DOI:10.1063/5.0101777

AIP Publishing

$U^{q\boldsymbol{\mu}} = U^{q\boldsymbol{\mu}}_{\mathrm{sr}} + U^{q\boldsymbol{\mu}}_{\mathrm{lr},0} + U^{q\boldsymbol{\mu}}_{\mathrm{lr},*}$. The single terms are written as

$$U^{q\boldsymbol{\mu}}_{\mathrm{sr}} = \frac{1}{2}\sum_{i=1}^{N_p}\sum_{J=1}^{N_d}\sum_{\boldsymbol{n}} \frac{q_i(\boldsymbol{r}_i - \boldsymbol{r}_J + \boldsymbol{m})\cdot\boldsymbol{\mu}_J}{|\boldsymbol{r}_i - \boldsymbol{r}_J + \boldsymbol{m}|^3}\left[\operatorname{erfc}\left[\alpha|\boldsymbol{r}_i - \boldsymbol{r}_J + \boldsymbol{m}|\right] + \frac{2\alpha}{\sqrt{\pi}}|\boldsymbol{r}_i - \boldsymbol{r}_J + \boldsymbol{m}|\exp\left[-\alpha^2|\boldsymbol{r}_i - \boldsymbol{r}_J + \boldsymbol{m}|^2\right]\right] \tag{12a}$$

$$U^{q\boldsymbol{\mu}}_{\mathrm{lr},0} = \frac{\pi}{L_x L_y}\sum_{i=1}^{N_p}\sum_{J=1}^{N_d} q_i \mu^z_J \operatorname{erf}\left[\alpha(z_i - z_J)\right] \tag{12b}$$

$$U^{q\boldsymbol{\mu}}_{\mathrm{lr},*} = -\frac{\mathrm{i}}{L_x L_y}\sum_{i=1}^{N_p}\sum_{J=1}^{N_d}\int_{-\infty}^{\infty}\mathrm{d}u\sum_{\boldsymbol{k}\neq 0} q_i(\boldsymbol{\mu}_J\cdot\boldsymbol{h} + \mu^z_J u)\frac{\exp\left[-\frac{h^2+u^2}{4\alpha^2}\right]}{h^2+u^2}\exp\left[\mathrm{i}\left(\boldsymbol{h}\cdot(\boldsymbol{r}_i - \boldsymbol{r}_J) + u(z_i - z_J)\right)\right] \tag{12c}$$

4. Gaussian charge-Gaussian charge interaction: U^{QQ}

The mutual interaction between Gaussian-distributed charges is also given in Ref. 15. Writing, as always, $U^{QQ} = U^{QQ}_{\mathrm{sr}} + U^{QQ}_{\mathrm{lr},0} + U^{QQ}_{\mathrm{lr},*} + U^{QQ}_{\mathrm{self}}$, we have

$$U^{QQ}_{\mathrm{sr}} = \frac{1}{2}\sum_{\alpha=1}^{N_g}\sum_{\beta=1}^{N_g}\sum_{\boldsymbol{n}}{}' \frac{Q_\alpha Q_\beta}{|\boldsymbol{R}_{\alpha\beta} + \boldsymbol{m}|}\left(\operatorname{erfc}\left[\alpha(|\boldsymbol{R}_{\alpha\beta} + \boldsymbol{m}|)\right] - \operatorname{erfc}\left[\eta_{\alpha\beta}(|\boldsymbol{R}_{\alpha\beta} + \boldsymbol{m}|)\right]\right) \tag{13a}$$

$$U^{QQ}_{\mathrm{lr},0} = -\frac{\sqrt{\pi}}{L_x L_y}\sum_{\alpha=1}^{N_g}\sum_{\beta=1}^{N_g} Q_\alpha Q_\beta\left(\frac{\exp\left[-\alpha^2 Z^2_{\alpha\beta}\right]}{\alpha} + \sqrt{\pi}Z_{\alpha\beta}\operatorname{erf}\left[\alpha Z_{\alpha\beta}\right]\right) \tag{13b}$$

$$U^{QQ}_{\mathrm{lr},*} = \frac{1}{L_x L_y}\sum_{\alpha=1}^{N_g}\sum_{\beta=1}^{N_g}\int_{-\infty}^{\infty}\mathrm{d}u\sum_{\boldsymbol{k}\neq 0} Q_\alpha Q_\beta\frac{\exp\left[-\frac{h^2+u^2}{4\alpha^2}\right]}{h^2+u^2}\exp\left[\mathrm{i}\left(\boldsymbol{h}\cdot\boldsymbol{R}_{\alpha\beta} + uZ_{\alpha\beta}\right)\right] \tag{13c}$$

$$U^{QQ}_{\mathrm{self}} = \left(\frac{\eta_\alpha}{\sqrt{2\pi}} - \frac{\alpha}{\sqrt{\pi}}\right)\sum_{\alpha=1}^{N_g} Q^2_\alpha \tag{13d}$$

In Eq. (13a) we defined $\eta_{\alpha\beta} \equiv \frac{\eta_\alpha\eta_\beta}{\sqrt{\eta^2_\alpha + \eta^2_\beta}}$. Also here, note that long-range interactions have the same form as in the case of the mutual interaction between point charges, with the integrated Gaussian charges in place of the point charges.

5. Gaussian charge-point dipole interaction: $U^{Q\boldsymbol{\mu}}$

As mentioned above, this term has never been reported in the literature. Its form is therefore derived in detail in the SM. Here we write $U^{Q\boldsymbol{\mu}} = U^{Q\boldsymbol{\mu}}_{\mathrm{sr}} + U^{Q\boldsymbol{\mu}}_{\mathrm{lr},0} + U^{Q\boldsymbol{\mu}}_{\mathrm{lr},*}$ with

$$\begin{aligned}U^{Q\boldsymbol{\mu}}_{\mathrm{sr}} = \frac{1}{2}\sum_{\alpha=1}^{N_g}\sum_{J=1}^{N_d}\sum_{\boldsymbol{n}} &\frac{Q_\alpha\boldsymbol{\mu}_J\cdot(\boldsymbol{R}_\alpha - \boldsymbol{r}_J + \boldsymbol{m})}{|\boldsymbol{R}_\alpha - \boldsymbol{r}_J + \boldsymbol{m}|^3}\times\\ \times&\Bigg[\operatorname{erfc}\left[\alpha|\boldsymbol{R}_\alpha - \boldsymbol{r}_J + \boldsymbol{m}|\right] + \frac{2\alpha}{\sqrt{\pi}}|\boldsymbol{R}_\alpha - \boldsymbol{r}_J + \boldsymbol{m}|\exp\left[-\alpha^2|\boldsymbol{R}_\alpha - \boldsymbol{r}_J + \boldsymbol{m}|^2\right]+\\ -&\left(\operatorname{erfc}\left[\eta_\alpha|\boldsymbol{R}_\alpha - \boldsymbol{r}_J + \boldsymbol{m}|\right] + \frac{2\eta_\alpha}{\sqrt{\pi}}|\boldsymbol{R}_\alpha - \boldsymbol{r}_J + \boldsymbol{m}|\exp\left[-\eta^2_\alpha|\boldsymbol{R}_\alpha - \boldsymbol{r}_J + \boldsymbol{m}|^2\right]\right)\Bigg]\end{aligned} \tag{14a}$$

$$U^{Q\boldsymbol{\mu}}_{\mathrm{lr},0} = \frac{\pi}{L_x L_y}\sum_{\alpha=1}^{N_g}\sum_{J=1}^{N_d} Q_\alpha \mu^z_J \operatorname{erf}\left[\alpha(Z_\alpha - z_J)\right] \tag{14b}$$

$$U^{Q\boldsymbol{\mu}}_{\mathrm{lr},*} = -\frac{\mathrm{i}}{L_x L_y}\sum_{\alpha=1}^{N_g}\sum_{J=1}^{N_d}\int_{-\infty}^{\infty}\mathrm{d}u\sum_{\boldsymbol{k}\neq 0} Q_\alpha(\boldsymbol{\mu}_J\cdot\boldsymbol{h} + \mu^z_J u)\frac{\exp\left[-\frac{h^2+u^2}{4\alpha^2}\right]}{h^2+u^2}\exp\left[\mathrm{i}\left(\boldsymbol{h}\cdot(\boldsymbol{R}_\alpha - \boldsymbol{r}_J) + u(Z_\alpha - z_J)\right)\right] \tag{14c}$$

Once again, Gaussian charges behave, in the long-range, as point charges equal to the integrated Gaussian charge (compare Eqs. (12b) and (12c) with Eqs. (14b) and (14c)).

6. Point dipole-point dipole interaction: $U^{\boldsymbol{\mu}\boldsymbol{\mu}}$

The last energy contribution for the model discussed in this paper is the mutual interaction between point dipoles. The expression for the 2D PBC case can be derived as the expression in the 3D PBC case given in Ref. 24. The interaction energy can be divided as $U^{\boldsymbol{\mu}\boldsymbol{\mu}} = U^{\boldsymbol{\mu}\boldsymbol{\mu}}_{\text{sr}} + U^{\boldsymbol{\mu}\boldsymbol{\mu}}_{\text{lr},0} + U^{\boldsymbol{\mu}\boldsymbol{\mu}}_{\text{lr},*} + U^{\boldsymbol{\mu}\boldsymbol{\mu}}_{\text{self}}$ and the single contributions are given by

$$U^{\boldsymbol{\mu}\boldsymbol{\mu}}_{\text{sr}} = \frac{1}{2}\sum_{I=1}^{N_d}\sum_{J=1}^{N_d}\sum_{\boldsymbol{n}}{}' \frac{\boldsymbol{\mu}_I \cdot S_{IJ} \cdot \boldsymbol{\mu}_J}{|\boldsymbol{r}_{IJ}+\boldsymbol{m}|^3}\left[\operatorname{erfc}\left[\alpha|\boldsymbol{r}_{IJ}+\boldsymbol{m}|\right] + \frac{2\alpha}{\sqrt{\pi}}|\boldsymbol{r}_{IJ}+\boldsymbol{m}|\exp\left[-\alpha^2|\boldsymbol{r}_{IJ}+\boldsymbol{m}|^2\right]\right] + \tag{15a}$$

$$- \frac{\left[\boldsymbol{\mu}_I \cdot (\boldsymbol{r}_{IJ}+\boldsymbol{m})\right]\left[\boldsymbol{\mu}_J \cdot (\boldsymbol{r}_{IJ}+\boldsymbol{m})\right]}{|\boldsymbol{r}_{IJ}+\boldsymbol{m}|^2}\frac{4\alpha^3}{\sqrt{\pi}}\exp\left[-\alpha^2|\boldsymbol{r}_{IJ}+\boldsymbol{m}|^2\right] \tag{15b}$$

$$U^{\boldsymbol{\mu}\boldsymbol{\mu}}_{\text{lr},0} = \frac{2\alpha\sqrt{\pi}}{L_x L_y}\sum_{I=1}^{N_d}\sum_{J=1}^{N_d}\mu_I^z\mu_J^z\exp\left[-\alpha^2 z_{IJ}^2\right] \tag{15c}$$

$$U^{\boldsymbol{\mu}\boldsymbol{\mu}}_{\text{lr},*} = \frac{1}{L_x L_y}\sum_{I=1}^{N_d}\sum_{J=1}^{N_d}\int_{-\infty}^{\infty}\mathrm{d}u\sum_{\boldsymbol{k}\neq 0}(\boldsymbol{\mu}_I\cdot\boldsymbol{h}+\mu_I^z u)(\boldsymbol{\mu}_J\cdot\boldsymbol{h}+\mu_J^z u)\frac{\exp\left[-\frac{h^2+u^2}{4\alpha^2}\right]}{h^2+u^2}\exp\left[\mathrm{i}\left(\boldsymbol{h}\cdot\boldsymbol{r}_{IJ}+u z_{IJ}\right)\right] \tag{15d}$$

$$U^{\boldsymbol{\mu}\boldsymbol{\mu}}_{\text{self}} = -\frac{2\alpha^3}{3\sqrt{\pi}}\sum_{I=1}^{N_d}\boldsymbol{\mu}_I^2 \tag{15e}$$

where the matrix S_{IJ} is defined by $S_{IJ}^{\xi\chi} = \delta^{\xi\chi} - \frac{3(\xi_{IJ}+m^{\xi})(\chi_{IJ}+m^{\chi})}{|\boldsymbol{r}_{IJ}^2+\boldsymbol{m}|}$ and $\xi_I, \chi_I \in \{x_I, y_I, z_I\}$. $\delta^{\xi\chi}$ is the Kroenecker's delta function, which is 1 if $\xi = \chi$ and 0 otherwise.

B. Implementation details

The long-range, $\boldsymbol{k} \neq 0$ terms introduced in the previous subsection are in general complex number due to the presence of the complex exponentials. Nonetheless, these can be transformed in purely real expressions exploiting the Euler's formula, i.e. $\exp[\mathrm{i}\phi] = \cos(\phi) + \mathrm{i}\sin(\phi)$. Let us note first that the problematic long-range terms can be grouped in two sets based on similarities in their structure. The first set consists of the terms $U^{qq}_{\text{lr},*}$, $U^{QQ}_{\text{lr},*}$, $U^{qQ}_{\text{lr},*}$ and $U^{\boldsymbol{\mu}\boldsymbol{\mu}}_{\text{lr},*}$. The only difference among these terms arise from the different "charges" (in some cases the point charge q_i, in others the integrated Gaussian charge Q_α or the scalar product between the dipole moment and the wavevector $\boldsymbol{\mu}_j \cdot \boldsymbol{h} + \mu_j^z u$) and the specific definitions of the distances at the exponent appearing in their expressions. A similar observation applies to the second set, composed by the terms $U^{q\boldsymbol{\mu}}_{\text{lr},*}$, $U^{Q\boldsymbol{\mu}}_{\text{lr},*}$. We discuss these two sets separately. About the former, exploiting the definition of the complex exponential, the parity of some of the trigonometrical functions with respect to the summation and integration interval and the trigonometrical expression of a difference, we obtain

$$U^{qq}_{\text{lr},*} = \frac{1}{L_x L_y}\int_{-\infty}^{\infty}\mathrm{d}u\sum_{\boldsymbol{k}\neq 0}\frac{\exp\left[-\frac{h^2+u^2}{4\alpha^2}\right]}{h^2+u^2}\left[\left[\sum_{i=1}^{N_p} q_i\cos(\boldsymbol{h}\cdot\boldsymbol{r}_i + u z_i)\right]^2 + \left[\sum_{j=1}^{N_p} q_j\sin(\boldsymbol{h}\cdot\boldsymbol{r}_j + u z_j)\right]^2\right] \tag{16a}$$

$$U^{qQ}_{\text{lr},*} = \frac{1}{L_x L_y}\int_{-\infty}^{\infty}\mathrm{d}u\sum_{\boldsymbol{k}\neq 0}\frac{\exp\left[-\frac{h^2+u^2}{4\alpha^2}\right]}{h^2+u^2}\left[\left[\sum_{i=1}^{N_p} q_i\cos(\boldsymbol{h}\cdot\boldsymbol{r}_i + u z_i)\right]^2 + \left[\sum_{\alpha=1}^{N_g} Q_\alpha\sin(\boldsymbol{h}\cdot\boldsymbol{R}_\alpha + u Z_\alpha)\right]^2\right] \tag{16b}$$

$$U^{QQ}_{\text{lr},*} = \frac{1}{L_x L_y}\int_{-\infty}^{\infty}\mathrm{d}u\sum_{\boldsymbol{k}\neq 0}\frac{\exp\left[-\frac{h^2+u^2}{4\alpha^2}\right]}{h^2+u^2}\left[\left[\sum_{\alpha=1}^{N_g} Q_\alpha\cos(\boldsymbol{h}\cdot\boldsymbol{R}_\alpha + u Z_\alpha)\right]^2 + \left[\sum_{\beta=1}^{N_g} Q_\beta\sin(\boldsymbol{h}\cdot\boldsymbol{R}_\beta + u Z_\beta)\right]^2\right] \tag{16c}$$

$$U^{\boldsymbol{\mu}\boldsymbol{\mu}}_{\text{lr},*} = \frac{1}{L_x L_y}\int_{-\infty}^{\infty}\mathrm{d}u\sum_{\boldsymbol{k}\neq 0}\frac{\exp\left[-\frac{h^2+u^2}{4\alpha^2}\right]}{h^2+u^2}\left[\left[\sum_{I=1}^{N_d}(\boldsymbol{\mu}_I\cdot\boldsymbol{h}+\mu_I^z u)\cos(\boldsymbol{h}\cdot\boldsymbol{r}_I + u z_I)\right]^2 + \left[\sum_{J=1}^{N_d}(\boldsymbol{\mu}_J\cdot\boldsymbol{h}+\mu_J^z u)\sin(\boldsymbol{h}\cdot\boldsymbol{r}_J + u z_J)\right]^2\right] \tag{16d}$$

The same kind of procedure can be performed on the second set noting, in addition, that $\mathrm{i}\exp[\mathrm{i}x] = \exp[\mathrm{i}(x+\frac{\pi}{2})] = \cos(x+\frac{\pi}{2}) + \mathrm{i}\sin(x+\frac{\pi}{2}) = \mathrm{i}\cos(x) - \sin(x)$. In this way we obtain

$$U^{q\boldsymbol{\mu}}_{\mathrm{lr},*} = \frac{1}{L_xL_y}\int_{-\infty}^{\infty}\mathrm{d}u\sum_{\boldsymbol{k}\neq 0}\frac{\exp\left[-\frac{h^2+u^2}{4\alpha^2}\right]}{h^2+u^2}\left[\left[\sum_{i=1}^{N_p} q_i\sin(\boldsymbol{h}\cdot\boldsymbol{r}_i+uz_i)\right]\left[\sum_{J=1}^{N_d}(\boldsymbol{\mu}_J\cdot\boldsymbol{h}+\mu^z_J u)\cos(\boldsymbol{h}\cdot\boldsymbol{r}_J+uz_J)\right]+\right.$$
$$\left.-\left[\sum_{i=1}^{N_p} q_i\cos(\boldsymbol{h}\cdot\boldsymbol{r}_i+uz_i)\right]\left[\sum_{J=1}^{N_d}(\boldsymbol{\mu}_J\cdot\boldsymbol{h}+\mu^z_J u)\sin(\boldsymbol{h}\cdot\boldsymbol{r}_J+uz_J)\right]\right] \tag{17a}$$

$$U^{Q\boldsymbol{\mu}}_{\mathrm{lr},*} = \frac{1}{L_xL_y}\int_{-\infty}^{\infty}\mathrm{d}u\sum_{\boldsymbol{k}\neq 0}\frac{\exp\left[-\frac{h^2+u^2}{4\alpha^2}\right]}{h^2+u^2}\left[\left[\sum_{\alpha=1}^{N_g} Q_\alpha\sin(\boldsymbol{h}\cdot\boldsymbol{R}_\alpha+uZ_\alpha)\right]\left[\sum_{J=1}^{N_d}(\boldsymbol{\mu}_J\cdot\boldsymbol{h}+\mu^z_J u)\cos(\boldsymbol{h}\cdot\boldsymbol{r}_J+uz_J)\right]+\right.$$
$$\left.-\left[\sum_{\alpha=1}^{N_g} Q_\alpha\cos(\boldsymbol{h}\cdot\boldsymbol{R}_\alpha+uZ_\alpha)\right]\left[\sum_{J=1}^{N_d}(\boldsymbol{\mu}_J\cdot\boldsymbol{h}+\mu^z_J u)\sin(\boldsymbol{h}\cdot\boldsymbol{r}_J+uz_J)\right]\right] \tag{17b}$$

The expressions in Eqs. (16) and (17) are purely real and can be handle with standard numerical libraries and operators.

C. Additional degrees of freedom

In the interaction potential, the induced dipoles represent the instantaneous polarization of a molecule or an ion, which fulfill the following expression at each timestep:

$$\boldsymbol{\mu}_J = \alpha_J\boldsymbol{E}_J = -\alpha_J\boldsymbol{\nabla}_J V(\boldsymbol{r}) \tag{18}$$

where α_J is the polarizability of atom J and $\boldsymbol{E}_J$ the electric field felt by the atom. The latter depends not only on the charges of the system but also on the other induced dipoles. In practice, instead of solving self-consistently the set of equations 18, most of the implementations are made by adding a polarization term to the energy, which is given by

$$U_{\mathrm{pol}} = \sum_{J=1}^{N_d}\frac{\boldsymbol{\mu}_J^2}{2\alpha_J} \tag{19}$$

In the absence of electrodes, the induced dipoles are then computed by minimizing $U_1 = U_{elec} + U_{\mathrm{pol}}$. However, in MetalWalls we also have to account for the fact that electrodes are set at constant potential. This condition reads

$$V(\boldsymbol{r}) = \Psi_{\Omega_\pm} \tag{20}$$

where $\boldsymbol{r}$ is a point in the regions $\Omega_\pm$ occupied by the positive or negative electrode and $\Psi_{\Omega_\pm}$ is the potential set in the corresponding electrode. The condition can be reformulated in terms of the Gaussian charges as

$$\frac{\partial U_{\mathrm{elec}}}{\partial Q_\alpha} = \Psi_\alpha. \tag{21}$$

with $\Psi_\alpha = \Psi_{\Omega_\pm}$ depending on the electrode in which α is located. In practice, in the absence of induced dipoles, this problem is solved by minimizing $U_2 = U_{\mathrm{elec}} - \sum_{\alpha=1}^{N_g}\Psi_\alpha Q_\alpha$.

Now the two systems of additional degrees of freedom are coupled: Since U_{elec} depends on both $\{\boldsymbol{\mu}_j\}_{j=1}^{N_d}$ and $\{Q_\alpha\}_{\alpha=1}^{N_g}$, the Gaussian charges values will depend on the induced dipoles and *vice versa*. The total quantity which is minimized is $U = U_{\mathrm{elec}} + U_{\mathrm{pol}} - \sum_{\alpha=1}^{N_g}\Psi_\alpha Q_\alpha$.

III. COMPUTATION OF INDUCED DIPOLES AND ELECTRODE CHARGES: THE PRECONDITIONED CONJUGATE GRADIENT

Induced dipoles and electrode charges are computed in the Born-Oppenheimer approximation: Their value is determined through a minimization procedure of the energy function with respect to the additional dynamical variables modeling these quantities. Contrary to existing literature, in which either the induced dipoles or the electrode charges were to be computed, in this paper the Born-Oppenheimer condition has to be satisfied for the set of additional dynamical variables which includes both the induced dipoles $\boldsymbol{\mu}$ and electrode charges Q. In other words, given the interaction energy $U(\boldsymbol{\mu}, Q|\boldsymbol{r}, \boldsymbol{R})$ as a function of $\boldsymbol{\mu}$ and Q and which depends parametrically on the electrolyte particles positions $\boldsymbol{r}$ and on the geometry of the electrodes placed at positions $\boldsymbol{R}$, the values of the dipoles and the electrode charges are found, for a given value of the parameters $\boldsymbol{r}$ and $\boldsymbol{R}$, as the solution of the equation

$$\arg\min_{\boldsymbol{\mu},Q} U(\boldsymbol{\mu}, Q|\boldsymbol{R}, \boldsymbol{r}) \tag{22}$$

This optimization problem, which is now formulated in the space of dimension $3N_d + N_g$, can be very demanding from a computational point of view and many different approaches have been proposed to tackle its solu-

The Journal of Chemical Physics ACCEPTED MANUSCRIPT
AIP Publishing
This is the author's peer reviewed, accepted manuscript. However, the online version of record will be different from this version once it has been copyedited and typeset.
PLEASE CITE THIS ARTICLE AS DOI:10.1063/5.0101777

tion.[15,28,39–41] For models such as those considered in this paper, in which the dependence of the energy function on the additional variables is quadratic, the conjugate gradient method[42,43] provides a good balance between accuracy and efficiency and it is the preferred choice nowadays. However, as the minimization procedure usually takes 90 % of the simulation time in a typical Born-Oppenheimer simulation, methods and algorithms to improve the convergence of the conjugate gradient procedure (or even replace it by a less costly method[28,40,44,45]) are still object of investigation.

For the minimization of quadratic functions of the form $U = \frac{1}{2}xAx + bx + c$ — which corresponds to finding the solution of the linear system of equations $Ax + b = 0$ — preconditioning the symmetric, positive-definite matrix A has proven to be an effective tool for improving the speed of convergence of the conjugate gradient algorithm. Indeed, the convergence of the algorithm depends mainly on the condition number of the matrix A (see Ref. 43) defined as the ratio between its maximum and minimum eigenvalues. The preconditioning procedure is a technique in which the optimization problem is transformed in an equivalent one, i.e. one that has the same solution, but where a matrix with a lower condition number is involved. In practice, this is done by noting that the solution of the equation $Ax + b = 0$ is the same of $P^{-1}(Ax + b) = 0$ where the *preconditioner* P is a matrix of the same dimensions of A. If the condition number of the matrix $P^{-1}A$ is lower than that of A the algorithm will be more efficient in solving the problem.

Unfortunately, a general strategy for finding a good preconditioner does not exist and the choice of an effective matrix P is highly system dependent. A quite common approach — even though sometimes ineffective — is to choose $P = \operatorname{diag} A$, the so-called Jacobi preconditioner.[46] This choice has the double advantage that, on the one hand, it is not necessary to store an additional entire matrix, but just a vector and, on the other, that the computation of P^{-1} is trivial. If effective, the Jacobi preconditioner is particularly well-suited for minimization problems in high-dimensional spaces. Other choices, sometimes more effective but at the same time more demanding numerically and in terms of required memory, are for example based on approximate inverses, (incomplete) Cholesky factorizations and domain decompositions.[46]

To investigate the effectiveness of the Jacobi preconditioner for electrochemical problems we study the properties of the matrix associated to the system described in Ref. 30. This system consists of constant potential aluminium elctrodes in contact with a molten salt (pure LiCl) in which the electrolyte ions are represented using a polarizable force field. While being very simple, this system , which can be effectively handled numerically, captures all the important features of electrochemical systems. A thorough study of the matrix requires its storage and analysis, a process that usually requires an order N^3 of operations, where $N \times N$ (with $N = 3N_d + N_g$) is the size of the A matrix. This is affordable for our chosen system.

For electrochemical systems in which either the electrode charges and the induced dipoles are considered as dynamical variables, the solution vector x can be ordered as

$$x = (\mu_1^x, \mu_2^x, \ldots, \mu_{N_d-1}^z, \mu_{N_d}^z, Q_1, \ldots, Q_{N_g}) \tag{23}$$

With this choice, the matrix A is represented,in block form, as

$$A = \begin{pmatrix} \nabla^2_{\boldsymbol{\mu\mu}} U & \nabla^2_{\boldsymbol{\mu} Q} U \\ \nabla^2_{Q\boldsymbol{\mu}} U & \nabla^2_{QQ} U \end{pmatrix} \tag{24}$$

where U is the interaction energy given in Eq. (8). The diagonal of this matrix, which represents the Jacobi preconditioner will then be given by

$$\begin{aligned} P &= \operatorname{diag} A \\ &= (\nabla^2_{\mu_1^x \mu_1^x} U, \ldots, \nabla^2_{\mu_{N_d}^z \mu_{N_d}^z} U, \nabla^2_{Q_1 Q_1} U, \ldots, \nabla^2_{Q_{N_g} Q_{N_g}} U) \end{aligned} \tag{25}$$

The analytic expression for P can be obtained starting from the Ewald decompositions given in the previous section. Assuming nearest-image convention, we then have

$$\begin{aligned} \nabla^2_{\mu_J^\xi \mu_J^\xi} U = {} & \frac{2}{L_x L_y} \sum_{\boldsymbol{k} \neq \boldsymbol{0}} \int_{-\infty}^{\infty} \mathrm{d}u \, \frac{\exp\left[-\frac{h^2+u^2}{4\alpha^2}\right]}{h^2 + u^2} (\kappa^\xi)^2 \\ & + \delta^{\xi z} \frac{4\sqrt{\pi}}{L_x L_y} \alpha - \frac{4\alpha^3}{3\sqrt{\pi}} + \frac{1}{\alpha_J} \end{aligned} \tag{26a}$$

$$\begin{aligned} \nabla^2_{Q_\alpha Q_\alpha} U = {} & \frac{2}{L_x L_y} \sum_{\boldsymbol{k} \neq \boldsymbol{0}} \int_{-\infty}^{\infty} \mathrm{d}u \, \frac{\exp\left[-\frac{h^2+u^2}{4\alpha^2}\right]}{h^2 + u^2} \\ & - \frac{2}{\alpha} \frac{\sqrt{\pi}}{L_x L_y} + \frac{2}{\sqrt{\pi}} \left(\frac{\eta_\alpha}{\sqrt{2}} - \alpha \right) \end{aligned} \tag{26b}$$

for $i = 1, \ldots, N_d$, $\xi \in \{x, y, z\}$ and $\alpha = 1, \ldots, N_g$. In the previous equation we have also defined the vector $\boldsymbol{\kappa} = (2\pi \frac{k_x}{L_x}, 2\pi \frac{k_y}{L_y}, u)$ and we remark the difference between the Ewald smearing parameter α, the polarizability α_j of the electrolyte polarizable atom j (defined in EQ. (18)) and the index α of the Gaussian-distributed charge as in Q_α and η_α. Also, $\delta^{\xi z}$ is the Kronecker delta. In Eq. (26), it is possible to recognize in both expressions the two terms arising from the long-range part of the Ewald decomposition ($\boldsymbol{k} = 0$ and $\boldsymbol{k} \neq 0$) and the term arising from the self-interaction term. In the expression relative to the induced dipoles, Eq. (26a), also the contribution due to the so-called “self-polarization” term is present.

In what follows, we show results for a 10 ps simulation of the system of aluminum electrodes and polarizable LiCl.[30] The polarizability of the lithium ion is set to $\alpha_{\mathrm{Li}} = 0.13\,\text{Å}^3$, while the one of chloride is set to $\alpha_{\mathrm{Cl}} = 2.96\,\text{Å}^3$ as reported in previous work.[47] Along the simulation, we sample the configuration of the electrolyte every 100 fs and we compute the condition number with ($P^{-1}A$ matrix) and without (A matrix) preconditioning. Results are shown in Figure 1. Note how the Jacobi preconditioner reduces the condition number of the problem by one order of magnitude. It is also interesting to check the behavior of the conjugate gradient algorithm for the configurations for which we computed the condition number of the matrix. Figure 2 shows the number of iterations needed for convergence of the algorithm for these configurations, again without and with preconditioning. As expected, Figures 1 and 2 confirm that to a lower condition number of the matrix corresponds a lower number of iterations of the conjugate gradient algorithm to reach convergence.

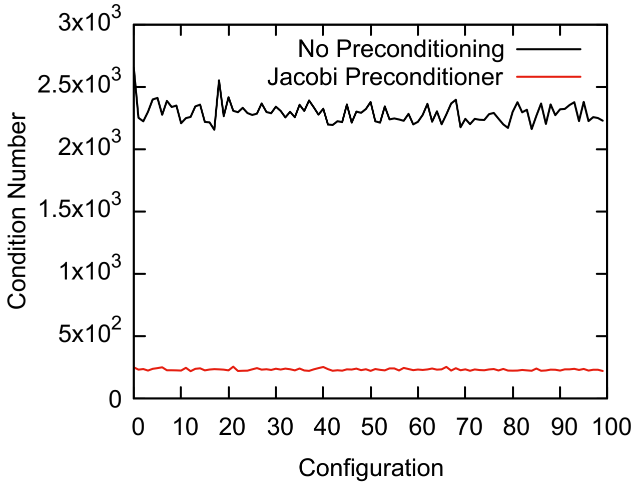

FIG. 1. Study of the condition number of the A matrix in Eq. (24) for the LiCl-Al system described in Ref. 30 with polarizable electrolyte (see text for further details). Configurations are sampled every 100 fs from a run of 10 ps of total length. The black solid line represents the condition number of the standard (not preconditioned) problem, while the red line provides the same quantity for the preconditioned problem, where Eqs. (26) have been used to compute the Jacobi preconditioner.

For larger systems such as the one discussed in Section V, where the study of the condition number is unfeasible due to the high dimensions of the matrix, the effectiveness of the Jacobi preconditioner can still be investigated by looking at the number of iterations to reach convergence. In Figure 3 we present this indicator for the LiCl-Al system, demonstrating that the Jacobi preconditioner reduces the number of iterations needed for convergence of the algorithm by roughly 50%.

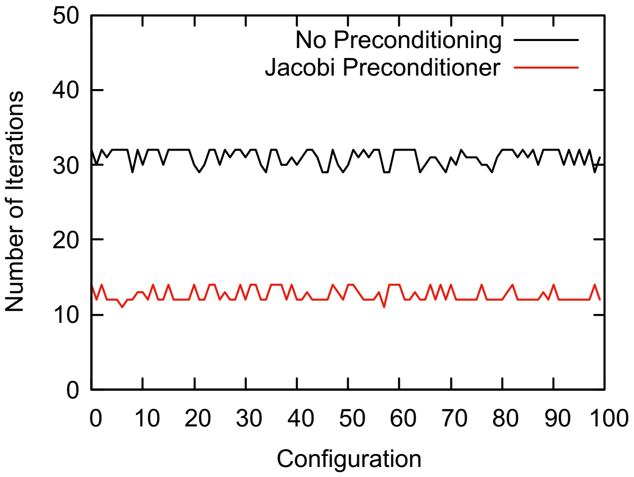

FIG. 2. Number of iterations needed to reach convergence of the conjugate gradient algorithm for the same system and the same configurations as in Fig. 1.

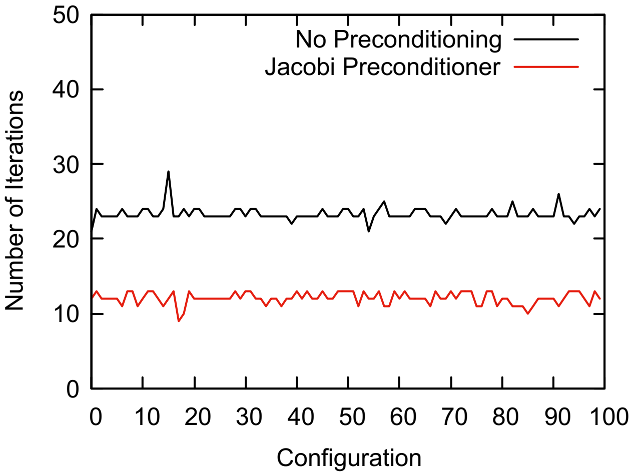

FIG. 3. Number of iterations needed to reach convergence of the conjugate gradient algorithm for the system described in Section V. Configurations are sampled every 10 fs on a 1 ps run. The black line represents the minimization procedure without preconditioning, while the red line represents preconditioned minimization where Jacobi preconditioner is computed via Eq. (26).

IV. VALIDATION ON SIMPLE SYSTEMS

A. Single dipole between single atom electrodes

A difficulty to validate the implementation of the expressions provided in Section II is that no other molecular dynamics code can be used to provide reference results. However, most of the terms were already derived and validated for 2D (U^{qq}, U^{qQ} and U^{QQ}) or 3D (U^{qq}, U^{qQ}, $U^{q\mu}$, U^{QQ} and $U^{\mu\mu}$) PBCs. The main validation test therefore concerns the $U^{Q\mu}$ term for which no results are available. To this end, we take advantage from the equivalence between an explicit dipoles and a set of two charges in the following.

In a first step, two systems composed of two single-atom electrodes placed in a box of dimension $L_x = L_y = 26.46\,\text{Å}$ and $L_z = 52.92\,\text{Å}$ were setup. In both cases, the first electrode is located at coordinates $(\frac{L_x}{2}; \frac{L_y}{2}; 0)$, while the second one is at $(\frac{L_x}{2}; \frac{L_y}{2}; L_z)$. These electrodes atoms have a Gaussian charge distribution width $\eta = 0.4\,\text{Å}^{-1}$, and the electrodes are held at a constant potential difference of 1 V. In the first system, which is referred to as a "point dipole system" in the following, a single atom is located in between the electrodes at coordinates $(\frac{L_x}{2}; \frac{L_y}{2}; z)$. This atom carries no charge but can be polarized, its polarizability being set to a value of $0.15\,\text{Å}^3$. The energy and the force acting on this atom are computed for different z coordinates. The second system mimics the first one, by introducing two central atoms $d_\mu = 0.53\,\text{Å}$ apart. They carry opposite charges, thus forming an explicit dipole which is placed in between the two electrodes. This system is thus called a "two-charges system". The charges on the atoms are taken from the value of the dipole moment μ obtained from the point dipole system at a similar z position. Charges $+q_\mu$ and $-q_\mu$ are assigned to the atoms of coordinates of $(\frac{L_x}{2}; \frac{L_y}{2}; z - \frac{d_\mu}{2})$ and $(\frac{L_x}{2}; \frac{L_y}{2}; z + \frac{d_\mu}{2})$, respectively. These atoms are not interacting with each other, so that from a physical point of view, the two systems are identical, but in the first setup the interaction potential only contains U^{QQ} and $U^{Q\mu}$ terms, while the second one contains U^{QQ} and U^{qQ}. The latter were already validated in numerous studies, so this allows us to directly test the new implementation.

For the Ewald summation, the cut-off distance for real space interactions is set to $r_{cut} = 12.70\,\text{Å}$. The relative error below which real-space and reciprocal-space terms are not included in the summation are set to 10^{-12}. Electroneutrality of the systems is enforced when computing the partial charges on the electrodes as described in Ref. 41. To compute energies and forces, the preconditioned conjugate gradient described in the previous section is used. The iterative process stops when: $|\text{residual}| < \text{tolerance} \times \sqrt{N_{atoms}}$, where tolerance is set at 10^{-12}. 151 calculations are performed with the z coordinate varying from 2.96 Å to 49.96 Å, with a step length of 0.31 Å to sample a large variation of the induced dipole moment.

Figure 4 shows the evolution of the energy (top) and of the force along z (bottom) for the point dipole system (black curve) and the two-charges system (orange dots). In the latter case, the force is obtained by summing the individual forces acting on each atom. The results for the two systems agree very well, with relative errors lower than 10^{-5} for the energies and lower than 2.5×10^{-2} for the forces. Additional tests were performed with varying values for the cut-off distance for the real space interactions, showing similar level of agreement.

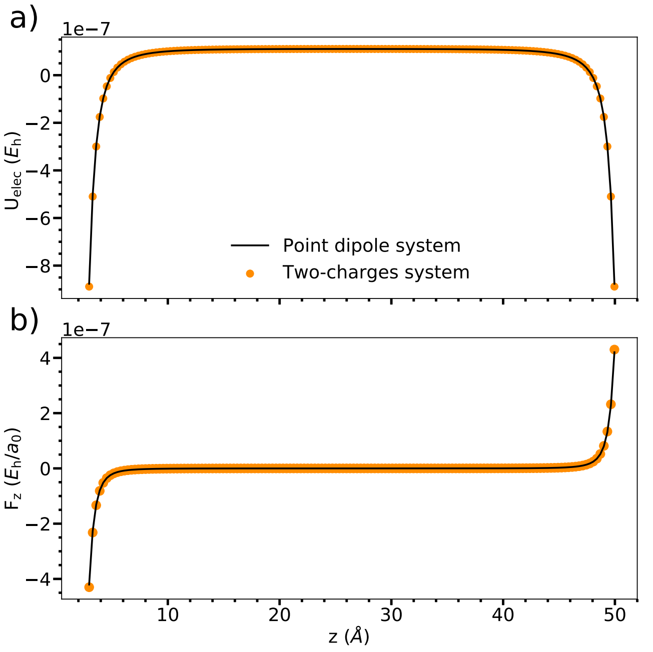

FIG. 4. Comparison of the energy and the force obtained for the point dipole and the two-charges system between single atom electrodes with an applied potential difference of 1 V. Energy (a) and force acting along the z direction on the atom(s) of interest (b) of the point dipole system (black curve) and of the two-charges system (orange dots). The relative error remains always lower than 10^{-5} and 2.5×10^{-2} for the energy and the force, respectively.

B. Single dipole between 100 atoms electrodes

In order to compare more precisely the charge distribution on the electrodes, another couple of systems were built in which the electrodes are made of a single plane of 100 atoms placed on a square lattice with a cell parameter of 2.94 Å. There again, the point dipole and the two-charges systems were set up for comparison. The parameters (electrode atoms Gaussian width, applied potential, Ewald real space cut-off, convergence of the conjugate gradient) were set similarly as for the single atom electrode tests. Figure 5 shows the charges on the electrode atoms for the two systems. Here also, a very good agreement is obtained, with a relative error lower than 10^{-8}, which confirms the validity of the expression derived for $U^{Q\mu}$ and its implementation in MetalWalls.

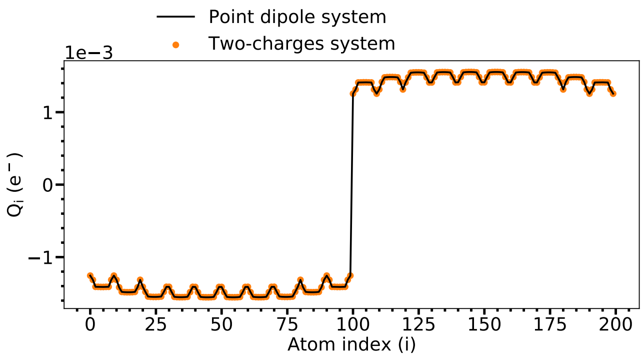

FIG. 5. Comparison of the charge on each atom of the electrodes obtained for the point dipole and the two-charges system between 100 atoms electrodes with an applied potential difference of 1 V. Electrode atoms are labeled by their index, with atoms 1 to 100 belonging to the first electrode and atoms 101 to 200 belonging to the second one. The maximum of the relative error obtained is lower than 10^{-8}.

V. VALIDATION ON A REALISTIC CAPACITOR

A. Simulation setup

Once the model has been validated for static calculations on model systems, it is also important to test the software on realistic cases. We have therefore chosen an already well-characterized system, composed of an ionic liquid between two graphite electrodes. This choice was made because, for such a system, it is possible to account in a mean-field way for polarization effects without including induced dipoles, by using reduced charges for all the ionic liquid atoms.[21] Such an approach was shown to yield correct structural properties, which provides us with a reference to compare with our polarizable force field simulations (other properties, in particular dynamic ones, may vary much more than the structural ones). We study an ionic liquid consisting of 322 ion pairs of 1-ethyl-3-methylimidazolium bis(trifluoromethylsulfonyl)imide (EMIM-TFSI). The two electrodes are at a distance of 10.9 nm and made of three parallel graphene sheets separated by 0.335 nm. The total dimensions of the box are $L_x = 3.408$ nm, $L_y = 3.689$ nm and $L_z = 11.38$ nm. Periodic boundary conditions have been applied in the x and y direction. A typical snapshot of the system is shown in Figure 6.

The CL&P[48,49] force-field is used for the non-polarizable simulation, with atomic charges scaled by a factor 0.8, as suggested in previous studies of the bulk liquid.[50–52] The polarizable simulations use an upgrade of the force-field (CL&Pol),[23,53,54] in which all atoms are polarizable except the hydrogen atoms. Note however that in the initial parameterization by Goloviznina *et al.*, the polarization effects were handled using Drude oscillators.[55] The corresponding parameters were therefore replaced by a polarizability in order to be used in our induced dipoles scheme. Atomic polarizabilities were taken from Schröder[56] following the CL&Pol methodology. In addition, short-range effects are handled a bit differently since we do not use Thole functions[57] for damping dipole-dipole interactions at short range. Instead, we use the conventional OPLS[58] rule for intramolecular charge-dipole and dipole-dipole interactions, *i.e.* they are set to 0 for nearest and second-nearest neighbors, while they are scaled by a factor 0.5 for atoms separated by two bonds. Concerning the intermolecular interactions, the charge-dipole interactions are damped at short-range using Tang-Toennies functions[59]

$$g^{ij}(r^{ij}) = 1 - c_D^{ij}\exp(-b_D^{ij}r^{ij})\sum_{k=0}^{4}\frac{(b_D^{ij}r^{ij})^k}{k!} \qquad (27)$$

where b_D^{ij} sets the range of the damping effect and c_D^{ij} the strength of the ion response.[22] All atom pairs ij have the same damping functions parameters, $b_D^{ij} = 1.06\,\text{Å}^{-1}$ and $c_D^{ij} = 0.53\,\text{Å}$. Simulations of the bulk liquid were performed in order to check that the so-modified polarizable force field yielded similar density, structural and diffusion properties as the original parameterization by Goloviznina *et al.*[23,53] The Lennard Jones parameters for the electrodes atoms are set to $\epsilon = 0.23$ kJ/mol and $\sigma = 3.37$ Å as in previous works[60]. The Lennard-Jones interactions are cut at 14.8 Å. The cut-off distance for real space interactions in the Ewald summation is set at $r_{cut} = 17$ Å. The relative error below which real-space term and reciprocal-space are not included in the summation is set to 10^{-5}.

The initial configuration was constructed using the PACKMOL software.[61] In order to obtain the correct liquid density, the electrodes were allowed to move in the z direction for few nanoseconds, by applying a pressure of 0 bar on both sides (free piston). When the electrode positions are stabilized, a bulk density of 1576 kg/m^3 is reached, which is close to the experimental value of 1526 kg/m^3 at 293.5 K.[62] Starting from this setup, a long simulation was performed using the non-polarizable interaction potential, from which three starting points were extracted. Three independent production trajectories were then performed using both the polarizable and non-polarizable potentials. These simulations were carried out for 20 ns, with a timestep of 2 fs and a temperature of 398 K. The latter value was chosen in order to accelerate the dynamics of the system and to converge the structure of the liquid within shorter simulations, since the objective of this work is to validate the code and not to do a specific study of the system. The two electrodes potential were fixed to 0 V. The systems were simulated in the NVT ensemble, using a Nosé-Hoover thermostat chain of length 5 with a relaxation time of 500 fs. In the following, the results were obtained by averaging over the three simulations for both polarizable or non-polarizable force-field.

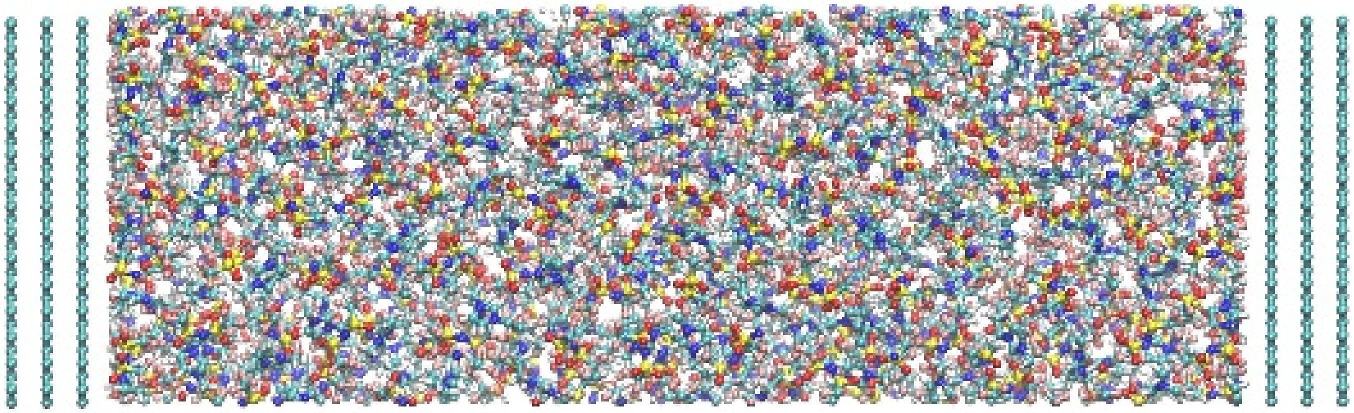

FIG. 6. Studied system composed of graphite electrodes separated by an ionic liquid (EMIM-TFSI). Green: C, blue: N, yellow: S, red: O, pink: F and white: H.

B. Results

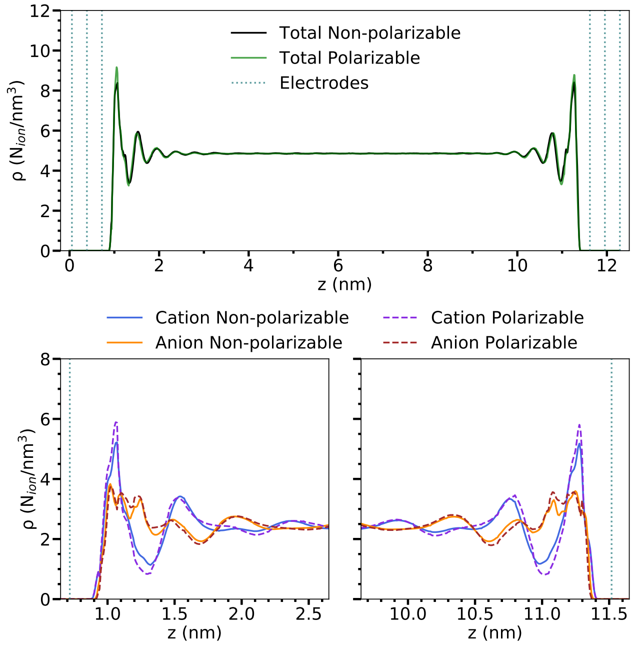

FIG. 7. Density profile for simulations including or not the polarization effects. Dotted lines show the position of the electrodes. The top panel shows the total density profiles, while the bottom panels show the density of anions and cations at the interfaces.

Figure 7 shows the number density profiles along the z direction for both force fields. For each ion type, the density is obtained by summing the averaged density of all atoms of the molecule, and normalized by the number of atoms of the ion. The top panel shows the total number of ions, and the bottom panels correspond to the EMIM$^+$ and TFSI$^-$ ions zoomed in at the interfaces. Electrode positions are shown as blue light vertical lines. Our results agree with the ones obtained in previous works, mainly with non-polarizable interaction potentials,[63–68] except for one study.[69] The structure is characterized by a strong ordering at the interface, with the formation of several layers in the vicinity of the electrode. We can conclude from these comparisons that our simulations with the polarizable force field yield the correct structure of the system. This indirect validation on a realistic system and the validations shown in the previous sections demonstrate the accuracy of the implementation of the polarization effects in conjunction with Gaussian charges in MetalWalls.

Despite yielding the same structure, it is likely that the different charge distributions in the two models will result in different electrostatic potentials at the interface. The latter can be computed as

$$\Psi(z) = \Psi_q(z) + \Psi_\mu(z) \tag{28}$$

where Ψ_q is the potential due to the charge distribution (from the electrolyte or electrode atoms) ρ_q and Ψ_μ is the one due to the z-component of the induced dipole moments distribution ρ_μ at a given position z,

$$\begin{aligned}\Psi_q(z) &= \Psi_q(z_0) - \frac{1}{\epsilon_0}\int_{z_0}^{z} dz' \int_{-\infty}^{z} dz'' \rho_q(z'') \\ \Psi_\mu(z) &= \Psi_\mu(z_0) + \frac{1}{\epsilon_0}\int_{z_0}^{z} dz' \rho_\mu(z')\end{aligned} \tag{29}$$

where ϵ_0 is the vacuum permittivity. The profiles are obtained by taking the reference point (z_0) inside the left electrode, so that $\Psi(z_0) = 0$. The variations of ρ_q, ρ_μ, and Ψ are shown for the non-polarizable and the polarizable models on Figure 8. The two charge distributions are of course very similar since the structure of the system does not differ much with the interaction potential. The main difference is the amplitude of the oscillations, which is reduced for the non-polarizable case due to the use of

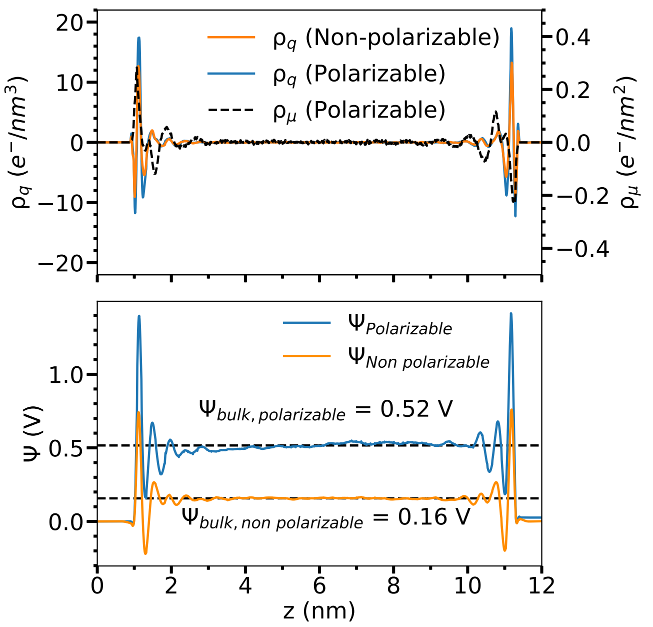

FIG. 8. Comparison of the charge and dipole densities (top) and electrical potential density (bottom) with and without polarizability, along the z direction. Atoms have large dipoles at the interfaces, but the average dipole value vanishes in the bulk. The bulk potential increases from 0.16 V to 0.52 V when adding the polarizability.

scaled charges. The dipole density also displays some peaks, the most intense corresponding to the layer of liquid closest to the electrodes in which a net polarization is observed. Interestingly, the positions of the peaks do not coincide with the ones obtained for the charge density and the oscillations seem to extend towards a longer distance away from the electrode, despite the shorter range of interactions involving dipoles. This is probably a consequence of the layered structure, which results in local polarization inside the layers.

A consequence of polarization effects is thus that the potential profiles differ markedly between the two cases. Although the peaks appear at the same positions, they have very different intensities. Consequently, the two models have different potentials of zero charge (PZC). This quantity can in principle be measured experimentally; it is defined as the potential difference between the bulk and the electrodes when the latter carry no net charge:[29]

$$\Delta\Psi_{\mathrm{PZC}} = \Psi_{electrode} - \Psi_{bulk} \tag{30}$$

In constant potential simulations, the PZC is readily obtained from the bulk potential on the profiles shown on Figure 8. We obtain a value of -0.16 V for the non-polarizable case and -0.52 V for the polarizable case, respectively. Our results show that this quantity mostly reflects the charge density distribution of the model, and not the structure of the liquid. It should therefore not be used to test the ability of a potential to predict the double-layer structure of a system with respect to experiments.

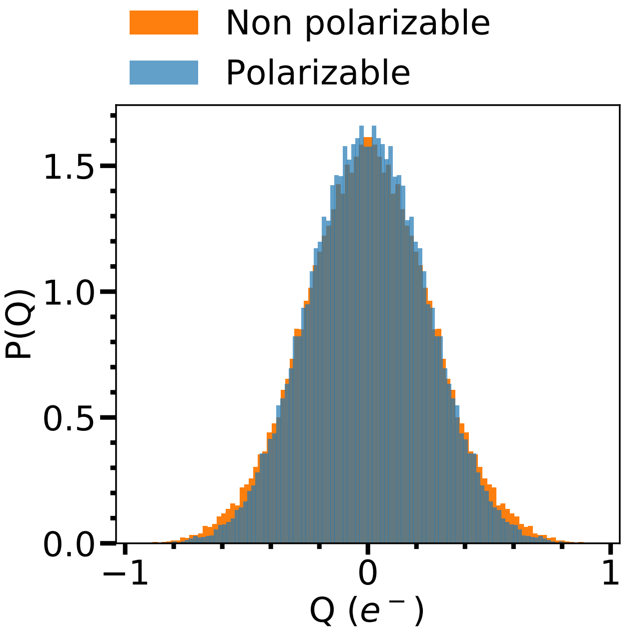

FIG. 9. Probabilities of the total charges on the electrodes for the non-polarizable and the polarizable models.

A much more robust test is to compute the capacitance of the system from the fluctuations of the total charge of the electrode according to Ref 41. Note that the contribution to the capacitance of the empty capacitor (*i.e.*, in the absence of liquid between the electrodes) is also taken into account. Figure 9 shows the probability to have a given total charge on the electrode for the two models. The distributions are very similar, which results in similar capacitances of $2.35 \pm 0.79\,\mu\mathrm{F/cm}^2$ for the non-polarizable case, and $2.03 \pm 0.42\,\mu\mathrm{F/cm}^2$ for the polarizable case. The fact that the same structure of the liquid yields similar results is a further (indirect) proof that the charges induced on the electrodes are correctly determined.

VI. ADSORPTION OF REDOX-FUNCTIONALIZED SPECIES ON GRAPHITE ELECTRODES

In this last section, we focus on an example for which polarization effects can only be represented via a suitable interaction potential. We simulate biredox ionic liquids, a new class of systems in which redox-active moieties are grafted to both the cationic and the anionic species.[70] Such systems have shown very promising results when employed in supercapacitors since they allow to markedly increase the amount of electricity stored in

The Journal of Chemical Physics ACCEPTED MANUSCRIPT

This is the author's peer reviewed, accepted manuscript. However, the online version of record will be different from this version once it has been copyedited and typeset.
PLEASE CITE THIS ARTICLE AS DOI:10.1063/5.0101777

AIP Publishing

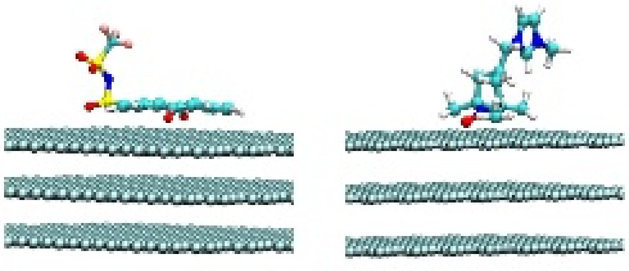

FIG. 10. Snapshots of the simulation showing the adsorption of the functionalized ionic liquid anion (left) and cation (right).

the devices with respect to conventional electrolytes such as ionic liquids.[71,72] However, their electricity storage mechanisms, in particular the interplay between capacitive and faradaic processes at the electrodes interfaces, remain to be solved.[73] Molecular dynamics can provide a microscopic view of the double-layer in such systems, but no accurate force field was previously available in the literature. Recently, we have developed a polarizable interaction potential for the redox active groups TEMPO and anthraquinone (AQ) based on electronic structure calculations,[35] which opens the way towards the simulation of biredox ionic liquids.

Here we simulate a system made of 10 biredox ionic liquid pairs, namely AQ-TFSI$^-$ and TEMPO-EMIM$^+$, mixed with 50 BMIM$^+$TFSI$^-$ ion pairs and 1624 acetonitrile molecules. The composition of the system was chosen according to previous experimental studies.[71] Each simulation was performed for 3.3 ns under a constant potential difference of either 0, 1 or 2 V in the NVT ensemble ($T = 298$ K). Two dimensional (2D) periodic boundary conditions were used, with box dimensions $L_x = 34.0$ Åand $L_y = 36.0$ Å, respectively. The electrodes separation has been fixed to 154.2 Å for which the density of the system in the middle of the box corresponds to the bulk value as in the previous section.

Although an extensive study of the system is out of the scope of the present work, we illustrate the software abilities by studying the adsorption mechanisms of redox-active molecules on the graphite electrodes, which impacts for example the kinetics of electron transfer. Firstly, we observe from the trajectory that the affinity of the ions for the electrode is similar for non-grafted and grafted species (within the statistical accuracy of the simulation, which is rather limited by the small number of ions in the simulation cells). However, as illustrated on the typical snapshots shown on Figure 10, the grafted ions tend to interact more strongly with the carbon surface through their redox-active moiety, leaving the ionic part of the molecule slightly behind the first plane. We can therefore expect a facilitated tunneling of the electrons when such liquids are used in supercapacitor devices.

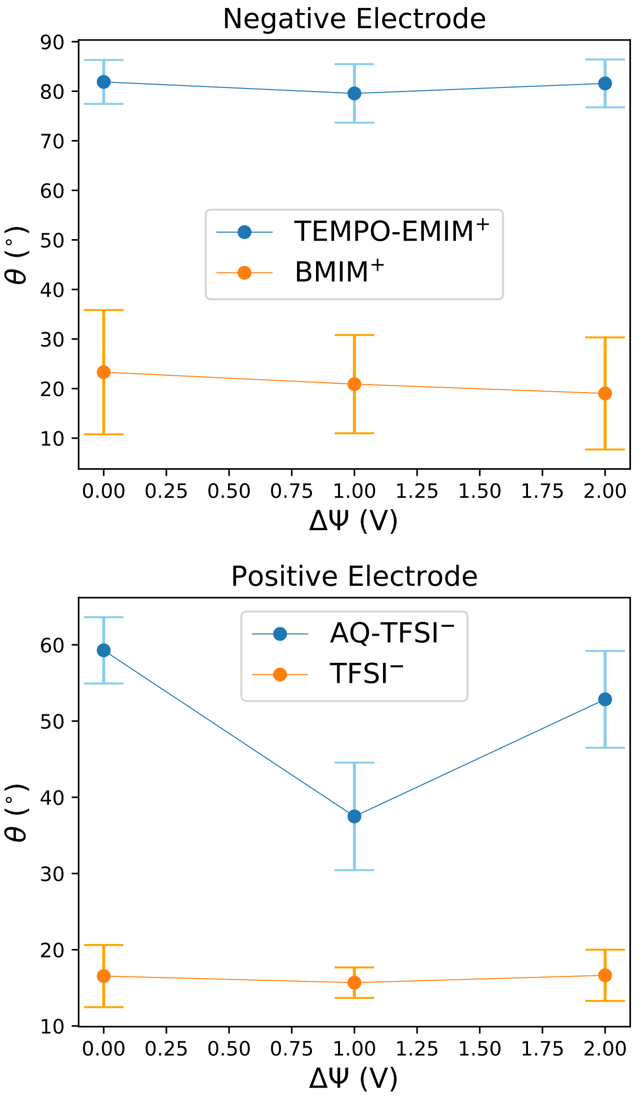

FIG. 11. Top: Angle between the normal to the plane of the imidazolium ring and the normal to the negative electrode at different potential difference for TEMPO-EMIM$^+$ and BMIM$^+$. Bottom : Angle between the vector connecting the two sulfur atoms and the projection of the normal to the plane of the positive electrode at different potential difference for AQ-TFSI$^-$ and TFSI$^-$. The error bars correspond to the standard deviation.

In order to get a more quantitative analysis, we study the orientation of the species at the interface. For each ion, we define a structural coordinate to analyze its orientation at the electrode. For the cation we choose the normal to the plane of the imidazolium ring and for the anion the vector between the two sulfur atoms. Then, we look at the angle between either the normal to the electrode plane and the normal to the plane of the imidazolium ring or the projection of the normal to the electrode plane and the vector connecting the two sulfur atoms. The averaged results over the trajectory are shown in Figure 11, for the different potential difference.

The Journal of Chemical Physics ACCEPTED MANUSCRIPT

This is the author's peer reviewed, accepted manuscript. However, the online version of record will be different from this version once it has been copyedited and typeset.
PLEASE CITE THIS ARTICLE AS DOI:10.1063/5.0101777

AIP Publishing

We can see that the redox functionalization of the ionic liquid changes the orientation at the electrode. In both cases, while the bare ions lie parallel to the surface, they become perpendicular in the biredox species. This effect reflects again the stronger affinity between graphite and redox moieties, which forces the ionic part of the molecules to adapt and change their orientation. Such an effect was not expected since the charged species are stabilized by the image charges in the metallic electrodes. The planar shape of the anthraquinone provides a lead for its affinity with graphite, since it may allow a more efficient packing, however it is not the case of the TEMPO group. Another possibility is that the polar C=O function of anthraquinone and N=O function of the TEMPO display a large interaction with the fluctuating charge of the metal. However, this would require costly additional simulations, and we leave this for future work.

VII. CONCLUSION

The simulation of electrochemical systems requires to account precisely for polarization effects at the electrode/electrolyte interface. By combining two sets of additional degrees of freedom, the induced dipoles in the liquid and the partial charges inside the electrode, MetalWalls now allows to use state-of-the-art force fields in such simulations. In this work, we have derived the equations enabling the simulation of systems including point charges, Gaussian charges and induced dipoles. Due to the long range nature of these interactions, it is necessary to use the Ewald summation method, which consists in the splitting the interaction potential in two sums, one in the real space and the other in reciprocal space. The expressions are provided for 2D periodic boundary conditions, which corresponds to the common setup for simulating electrochemical systems. The additional degrees of freedom are computed through a conjugate gradient minimization procedure, whose computational cost can be decreased through the use of simple preconditioning techniques. Note that another common approach, which consists in using 3D PBCs with an additional (large) vacuum region and adding a correction term for the slab geometry is also implemented in MetalWalls. Although this allows to reduce the computational time, as noted in a recent work this setup should be used with caution when used for simulating constant potential electrodes.[19]

We have then validated the implementation of the formulae for 2D PBC. This cannot be done through a simple comparison with other codes since the above features are not yet included elsewhere. We therefore focused first on a simple system consisting of a single dipole between electrodes, for which the dipole can be replaced by a couple of explicit charges, providing reference results. We then compare the results obtained on lengthy simulations of a realistic system, the EMIM-TFSI ionic liquid in contact with graphite electrodes. This system was chosen because it is possible to account effectively for the polarization of the electrolyte using rescaled charges. The simulations yield similar structure for the interfacial liquid and the capacitance as expected.

The capabilities of MetalWalls were then demonstrated by simulating a system for which no non-polarizable force field exists. It consists in a pair of redox-functionalized ions dissolved in a conventional electrolyte, again in contact with graphite electrodes. The structural analysis showed that the redox moieties impact the adsorption of molecules at the surface of the electrode, providing a basis for the understanding of the properties of these electrolytes in future works.

Although this work only focused on simple electrode geometries, the methods presented here are general and can be applied to any electrode geometry. MetalWalls can therefore be used to simulated complex systems, such as slit nanopores, carbide-derived carbons, etc. It is parallelized using MPI for conventional CPU-based high performance computers and OpenACC for GPU, so that typical system sizes of 10,000 to 50,000 atoms can be simulated routinely. MetalWalls is therefore a valuable tool for the characterization of the structure of the electrolyte in many electrochemical devices, such as supercapacitors,[60] batteries,[74] electrocatalyzers,[75] etc. The next challenge will be to develop the adequate force fields for such systems. There are currently many developments aiming at accounting for the different metallicities of the electrode materials,[36,76,77] but there is no systematic recipe for choosing the corresponding parameters. Approaches based on high-level *ab initio* calculations will certainly provide an important input towards this direction.[78,79]

SUPPLEMENTARY MATERIAL

The supplementary material contains the complete derivation of 2D-PBC Ewald decomposition for energy and forces of Gaussian charges-point dipoles term and the Ewald decomposition for the forces.

ACKNOWLEDGMENTS

We thank Paul Madden for initiating the MetalWalls project and for many fruitful discussions. This project has received funding from the European Research Council (ERC) under the European Union's Horizon 2020 research and innovation programme (grant agreements No. 771294 and 863473). This work was granted access to the HPC resources of CINES under Allocation A0120910463 made by GENCI. We acknowledge support from EoCoE, a project funded by the European Union Contracts No. H2020-EINFRA-2015-1-676629 and H2020-INFRAEDI-2018-824158.

DATA AVAILABILITY

The MetalWalls code is openly available in the repository https://gitlab.com/ampere2/metalwalls.

[1] N. Yao, X. Chen, Z.-H. Fu, and Q. Zhang, "Applying classical, ab initio, and machine-learning molecular dynamics simulations to the liquid electrolyte for rechargeable batteries," Chem. Rev. **122**, 10970–11021 (2022).

[2] R. E. Warburton, A. V. Soudackov, and S. Hammes-Schiffer, "Theoretical modeling of electrochemical proton-coupled electron transfer," Chem. Rev. **122**, 10599–10650 (2022).

[3] A. Groß and S. Sakong, "Ab initio simulations of water/metal interfaces," Chem. Rev. **122**, 10746–10776 (2022).

[4] X. Zhao, Z. H. Levell, S. Yu, and Y. Liu, "Atomistic understanding of two-dimensional electrocatalysts from first principles," Chem. Rev. **122**, 10675–10709 (2022).

[5] F. Dattila, R. R. Seemakurthi, Y. Zhou, and N. López, "Modeling operando electrochemical CO_2 reduction," Chem. Rev. **122**, 11085–11130 (2022).

[6] G. Jeanmairet, B. Rotenberg, and M. Salanne, "Microscopic simulations of electrochemical double-layer capacitors," Chem. Rev. **122**, 10860–10898 (2022).

[7] A. Van der Ven, Z. Deng, S. Banerjee, and S. P. Ong, "Rechargeable alkali-ion battery materials: Theory and computation," Chem. Rev. **120**, 6977–7019 (2020).

[8] D. Bedrov, J.-P. Piquemal, O. Borodin, A. D. MacKerell, Jr., B. Roux, and C. Schröder, "Molecular dynamics simulations of ionic liquids and electrolytes using polarizable force fields," Chem. Rev. **119**, 7940–7995 (2019).

[9] L. Scalfi, M. Salanne, and B. Rotenberg, "Molecular simulation of electrode-solution interfaces," Ann. Rev. Phys. Chem. **72**, 189–212 (2021).

[10] A. A. Kornyshev, "Double-layer in ionic liquids: paradigm change?" J. Phys. Chem. B **111**, 5545–5557 (2007).

[11] C.-Y. Li, J.-B. Le, Y.-H. Wang, S. Chen, Z.-L. Yang, J.-F. Li, J. Cheng, and Z.-Q. Tian, "In situ probing electrified interfacial water structures at atomically flat surfaces," Nat. Mater. **18**, 697–701 (2019).

[12] J. I. Siepmann and M. Sprik, "Influence of surface topology and electrostatic potential on water/electrode systems," J. Chem. Phys. **102**, 511–524 (1995).

[13] I. C. Yeh and M. L. Berkowitz, "Ewald summation for systems with slab geometry," J. Chem. Phys. **111**, 3155–3162 (1999).

[14] J. B. Haskins and J. W. Lawson, "Evaluation of molecular dynamics simulation methods for ionic liquid electric double layers," J. Chem. Phys. **144**, 134701 (2016).

[15] S. K. Reed, O. J. Lanning, and P. A. Madden, "Electrochemical interface between an ionic liquid and a model metallic electrode," J. Chem. Phys. **126**, 084704 (2007).

[16] T. R. Gingrich and M. Wilson, "On the ewald summation of gaussian charges for the simulation of metallic surfaces," Chem. Phys. Lett. **500**, 178–183 (2010).

[17] Z. Wang, Y. Yang, D. L. Olmsted, M. Asta, and B. B. Laird, "Evaluation of the constant potential method in simulating electric double-layer capacitors," J. Chem. Phys. **141**, 184102 (2014).

[18] S. Plimpton, "Fast Parallel Algorithms for Short-Range Molecular Dynamics," J. Comput. Phys. **117**, 1–19 (1995).

[19] L. J. V. Ahrens-Iwers and R. H. Meißner, "Constant potential simulations on a mesh," J. Chem. Phys. **155**, 104104 (2021).

[20] S. R. Tee and D. J. Searles, "Fully periodic, computationally efficient constant potential molecular dynamics simulations of ionic liquid supercapacitors," J. Chem. Phys. **156**, 184101 (2022).

[21] C. Schröder and O. Steinhauser, "Simulating polarizable molecular ionic liquids with drude oscillators," J. Chem. Phys. **133**, 154511 (2010).

[22] M. Salanne, "Simulations of Room Temperature Ionic Liquids: from Polarizable to Coarse-Grained Force Fields," Phys. Chem. Chem. Phys. **17**, 14270–14279 (2015).

[23] K. Goloviznina, J. N. C. Lopes, M. C. Gomes, and A. A. H. Pádua, "Transferable, polarizable force field for ionic liquids," J. Chem. Theory Comput. **15**, 5858–5871 (2019).

[24] A. Aguado and P. A. Madden, "Ewald summation of electrostatic multipole interactions up to the quadrupolar level," J. Chem. Phys. **119**, 7471–7483 (2003).

[25] N. Ohtori, M. Salanne, and P. A. Madden, "Calculations of the thermal conductivities of ionic materials by simulation with polarizable interaction potentials," J. Chem. Phys. **130**, 104507 (2009).

[26] M. Pounds, *Electrochemical charge transfer at a metallic electrode: a simulation study*, Ph.D. thesis, University of Edinburgh (2009).

[27] A. Coretti, S. Bonella, and G. Ciccotti, "Communication: Constrained molecular dynamics for polarizable models," J. Chem. Phys. **149**, 191102 (2018).

[28] A. Coretti, L. Scalfi, C. Bacon, B. Rotenberg, R. Vuilleumier, G. Ciccotti, M. Salanne, and S. Bonella, "Mass-zero constrained molecular dynamics for electrode charges in simulations of electrochemical systems," J. Chem. Phys. **152**, 194701 (2020).

[29] M. Pounds, S. Tazi, M. Salanne, and P. A. Madden, "Ion adsorption at a metallic electrode: an ab initio based simulation study," J. Phys: Condens. Matter **21**, 424109 (2009).

[30] S. Tazi, M. Salanne, C. Simon, P. Turq, M. Pounds, and P. A. Madden, "Potential-induced ordering transition of the adsorbed layer at the ionic liquid / electrified metal interface," J. Phys. Chem. B **114**, 8453–8459 (2010).

[31] F. Wang, O. Borodin, M. S. Ding, M. Gobet, J. Vatamanu, X. Fan, T. Gao, N. Edison, Y. Liang, S. Greenbaum, K. Xu, and C. Wang, "Hybrid Aqueous/Non-aqueous Electrolyte for Safe and High-Energy Li-Ion Batteries," Joule **2**, 927–937 (2018).

[32] D. T. Margul and M. E. Tuckerman, "A stochastic, resonance-free multiple time-step algorithm for polarizable models that permits very large time steps," J. Chem. Theory Comput. **12**, 2170–2180 (2016).

[33] P. Monmarché, J. Weisman, L. Lagardère, and J.-P. Piquemal, "Velocity jump processes: an alternative to multi-timestep methods for faster and accurate molecular dynamics simulations," J. Chem. Phys. **153**, 024101 (2020).

[34] A. Marin-Laflèche, M. Haefele, L. Scalfi, A. Coretti, T. Dufils, G. Jeanmairet, S. K. Reed, A. Serva, R. Berthin, C. Bacon, S. Bonella, B. Rotenberg, P. A. Madden, and M. Salanne, "Metalwalls: A classical molecular dynamics software dedicated to the simulation of electrochemical systems," J. Open Source Softw. **5**, 2373 (2020).

[35] R. Berthin, A. Serva, K. G. Reeves, E. Heid, C. Schröder, and M. Salanne, "Solvation of anthraquinone and tempo redox-active species in acetonitrile using a polarizable force field," J. Chem. Phys. **155**, 074504 (2021).

[36] A. Serva, L. Scalfi, B. Rotenberg, and M. Salanne, "Effect of the metallicity on the capacitance of gold-aqueous sodium choloride interfaces," J. Chem. Phys. **155**, 044703 (2021).

[37] A. Aguado, L. Bernasconi, and P. A. Madden, "Interionic potentials from *ab initio* molecular dynamics: The alkaline earth oxides CaO, SrO, and BaO," J. Chem. Phys. **118**, 5704–5717 (2003).

[38] M. Neumann, "Dipole moment fluctuation formulas in computer simulations of polar systems," Mol. Phys. **50**, 841–858 (1983).

[39] M. Sprik and M. L. Klein, "A polarizable model for water using distributed charge sites," J. Chem. Phys. **89**, 7556–7560 (1988).

[40] J. Kolafa, "Time-reversible always stable predictor-corrector method for molecular dynamics of polarizable molecules," J. Comput. Chem. **25**, 335–342 (2004).

[41] L. Scalfi, D. T. Limmer, A. Coretti, S. Bonella, P. A. Madden, M. Salanne, and B. Rotenberg, "Charge fluctuations from molecular simulations in the constant-potential ensemble," Phys. Chem. Chem. Phys. **22**, 10480–10489 (2020).

[42] W. H. Press, B. P. Flannery, S. A. Teukolsky, and W. T. Vetterling, *Numerical recipes in C: The art of scientific computing* (Cambridge University Press, Cambridge Cambridgeshire New

York, 1992).

[43] J. Nocedal and S. J. Wright, *Numerical optimization* (Springer, New York, 2006).

[44] T. D. Kühne, M. Krack, F. R. Mohamed, and M. Parrinello, "Efficient and accurate Car–Parrinello-like approach to Born–Oppenheimer molecular dynamics," Phys. Rev. Lett. **98**, 066401 (2007).

[45] F. Aviat, A. Levitt, B. Stamm, Y. Maday, P. Ren, J. W. Ponder, L. Lagardère, and J.-P. Piquemal, "Truncated conjugate gradient: An optimal strategy for the analytical evaluation of the many-body polarization energy and forces in molecular simulations," J. Chem. Theory Comput. **13**, 180–190 (2017).

[46] G. Golub and C. Van Loan, *Matrix Computations*, Johns Hopkins Studies in the Mathematical Sciences (Johns Hopkins University Press, 2013).

[47] Y. Ishii, S. Kasai, M. Salanne, and N. Ohtori, "Transport coefficients and the stokes–einstein relation in molten alkali halides with polarisable ion model," Mol. Phys. **113**, 2442–2450 (2015).

[48] J. N. C. Lopes and A. A. H. Pádua, "Molecular force field for ionic liquids composed of triflate or bistriflimide anions," J. Phys. Chem. B **108**, 16893–16898 (2004).

[49] J. N. C. Lopes, J. Deschamps, and A. A. H. Pádua, "Modeling ionic liquids using a systematic all-atom force field," J. Phys. Chem. B **108**, 11250–11250 (2004).

[50] V. Chaban, "Polarizability versus mobility: atomistic force field for ionic liquids," Phys. Chem. Chem. Phys. **13**, 16055–16062 (2011).

[51] B. L. Bhargava and S. Balasubramanian, "Refined potential model for atomistic simulations of ionic liquid [bmim][PF6]," J. Chem. Phys. **127**, 114510 (2007).

[52] Y. Zhang and E. J. Maginn, "A simple AIMD approach to derive atomic charges for condensed phase simulation of ionic liquids," J. Phys. Chem. B **116**, 10036–10048 (2012).

[53] K. Goloviznina, Z. Gong, M. F. Costa Gomes, and A. A. H. Pádua, "Extension of the cl&pol polarizable force field to electrolytes, protic ionic liquids, and deep eutectic solvents," J. Chem. Theory Comput. **17**, 1606–1617 (2021).

[54] K. Goloviznina, Z. Gong, and A. A. H. Padua, "The cl&pol polarizable force field for the simulation of ionic liquids and eutectic solvents," Wiley Interdiscip. Rev. Comput. Mol. Sci. , e1572 (2021).

[55] P. Drude, *The theory of optics* (Courier Dover Publications, 1901).

[56] E. Heid, A. Szabadi, and C. Schröder, "Quantum mechanical determination of atomic polarizabilities of ionic liquids," Phys. Chem. Chem. Phys. **20**, 10992–10996 (2018).

[57] B. T. Thole, "Molecular polarizabilities calculated with a modified dipole interaction," Chem. Phys. **59**, 341–350 (1981).

[58] W. L. Jorgensen, D. S. Maxwell, and J. Tirado-Rives, "Development and testing of the opls all-atom force field on conformational energetics and properties of organic liquids," J. Am. Chem. Soc. **118**, 11225–11236 (1996).

[59] K. T. Tang and J. P. Toennies, "An improved simple model for the van der waals potential based on universal damping functions for the dispersion coefficients," J. Chem. Phys. **80**, 3726–3741 (1984).

[60] C. Merlet, B. Rotenberg, P. A. Madden, P.-L. Taberna, P. Simon, Y. Gogotsi, and M. Salanne, "On the molecular origin of supercapacitance in nanoporous carbon electrodes," Nat. Mater. **11**, 306–310 (2012).

[61] L. Martínez, R. Andrade, E. G. Birgin, and J. M. Martínez, "PACKMOL: A package for building initial configurations for molecular dynamics simulations," J. Comput. Chem. **30**, 2157–2164 (2009).

[62] R. L. Gardas, M. G. Freire, P. J. Carvalho, I. M. Marrucho, I. M. A. Fonseca, A. G. M. Ferreira, and J. A. P. Coutinho, "$P\rho t$ measurements of imidazolium-based ionic liquids," J. Chem. Eng. Data **52**, 1881–1888 (2007).

[63] G. Feng, S. Li, W. Zhao, and P. T. Cummings, "Microstructure of room temperature ionic liquids at stepped graphite electrodes," AIChE J. **61**, 3022–3028 (2015).

[64] A. Fang and A. Smolyanitsky, "Simulation study of the capacitance and charging mechanisms of ionic liquid mixtures near carbon electrodes," J. Phys. Chem. C **123**, 1610–1618 (2019).

[65] P. S. Gil, S. J. Jorgenson, A. R. Riet, and D. J. Lacks, "Relationships between molecular structure, interfacial structure, and dynamics of ionic liquids near neutral and charged surfaces," J. Phys. Chem. C **122**, 27462–27468 (2018).

[66] S. Li, Z. Zhao, and X. Liu, "Electric double layer structure and capacitance of imidazolium-based ionic liquids with FSI- and tf-anions at graphite electrode by molecular dynamic simulations," J. Electroanal. Chem **851**, 113452 (2019).

[67] N. N. Rajput, J. Monk, R. Singh, and F. R. Hung, "On the influence of pore size and pore loading on structural and dynamical heterogeneities of an ionic liquid confined in a slit nanopore," J. Phys. Chem. C **116**, 5169–5181 (2012).

[68] J. Vatamanu, O. Borodin, D. Bedrov, and G. D. Smith, "Molecular dynamics simulation study of the interfacial structure and differential capacitance of alkylimidazolium bis(trifluoromethanesulfonyl)imide [cnmim][TFSI] ionic liquids at graphite electrodes," J. Phys. Chem. C **116**, 7940–7951 (2012).

[69] Z. Hu, J. Vatamanu, O. Borodin, and D. Bedrov, "A comparative study of alkylimidazolium room temperature ionic liquids with FSI and TFSI anions near charged electrodes," Electrochim. Acta **145**, 40–52 (2014).

[70] E. Mourad, L. Coustan, S. A. Freunberger, A. Mehdi, A. Vioux, F. Favier, and O. Fontaine, "Biredox ionic liquids: electrochemical investigation and impact of ion size on electron transfer," Electrochim. Acta **206**, 513–523 (2016).

[71] E. Mourad, L. Coustan, P. Lannelongue, D. Zigah, A. Mehdi, A. Vioux, S. A. Freunberger, F. Favier, and O. Fontaine, "Biredox ionic liquids with solid-like redox density in the liquid state for high-energy supercapacitors," Nat. Mater. **16**, 446–453 (2017).

[72] C. Bodin, E. Mourad, D. Zigah, S. Le Vot, S. A. Freunberger, F. Favier, and O. Fontaine, "Biredox ionic liquids: new opportunities toward high performance supercapacitors," Faraday Discuss. **206**, 393–404 (2018).

[73] O. Fontaine, "A deeper understanding of the electron transfer is the key to the success of biredox ionic liquids," Ener. Storage Mater. **21**, 240–245 (2019).

[74] P. Lemaire, A. Serva, M. Salanne, G. Rousse, H. Perrot, O. Sel, and J.-M. Tarascon, "Probing the electrode-electrolyte interface of a model k-ion battery electrode–the origin of rate capability discrepancy between aqueous and non-aqueous electrolytes," ACS Appl. Mater. Interfaces **14**, 20835–20847 (2022).

[75] N. Dubouis, A. Serva, R. Berthin, G. Jeanmairet, B. Porcheron, E. Salager, M. Salanne, and A. Grimaud, "Tuning water reduction through controlled nanoconfinement within an organic liquid matrix," Nat. Catal. **3**, 656–663 (2020).

[76] L. Scalfi, T. Dufils, K. G. Reeves, B. Rotenberg, and M. Salanne, "A semiclassical Thomas–Fermi model to tune the metallicity of electrodes in molecular simulations," J. Chem. Phys. **153**, 174704 (2020).

[77] A. Schlaich, D. Jin, L. Bocquet, and B. Coasne, "Electronic screening using a virtual thomas–fermi fluid for predicting wetting and phase transitions of ionic liquids at metal surfaces," Nat. Mater. **21**, 237–245 (2022).

[78] P. Clabaut, P. Fleurat-Lessard, C. Michel, and S. N. Steinmann, "Ten Facets, One Force Field: The GAL19 Force Field for Water-Noble Metal Interfaces," J. Chem. Theory Comput. **16**, 4565–4578 (2020).

[79] M. Ruggeri, K. Reeves, T.-Y. Hsu, G. Jeanmairet, M. Salanne, and C. Pierleoni, "Multi-scale simulation of the adsorption of lithium ion on graphite surface: from quantum monte carlo to molecular density functional theory," J. Chem. Phys. **156**, 094709 (2022).

Accepted to J. Chem. Phys. 10.1063/5.0101777

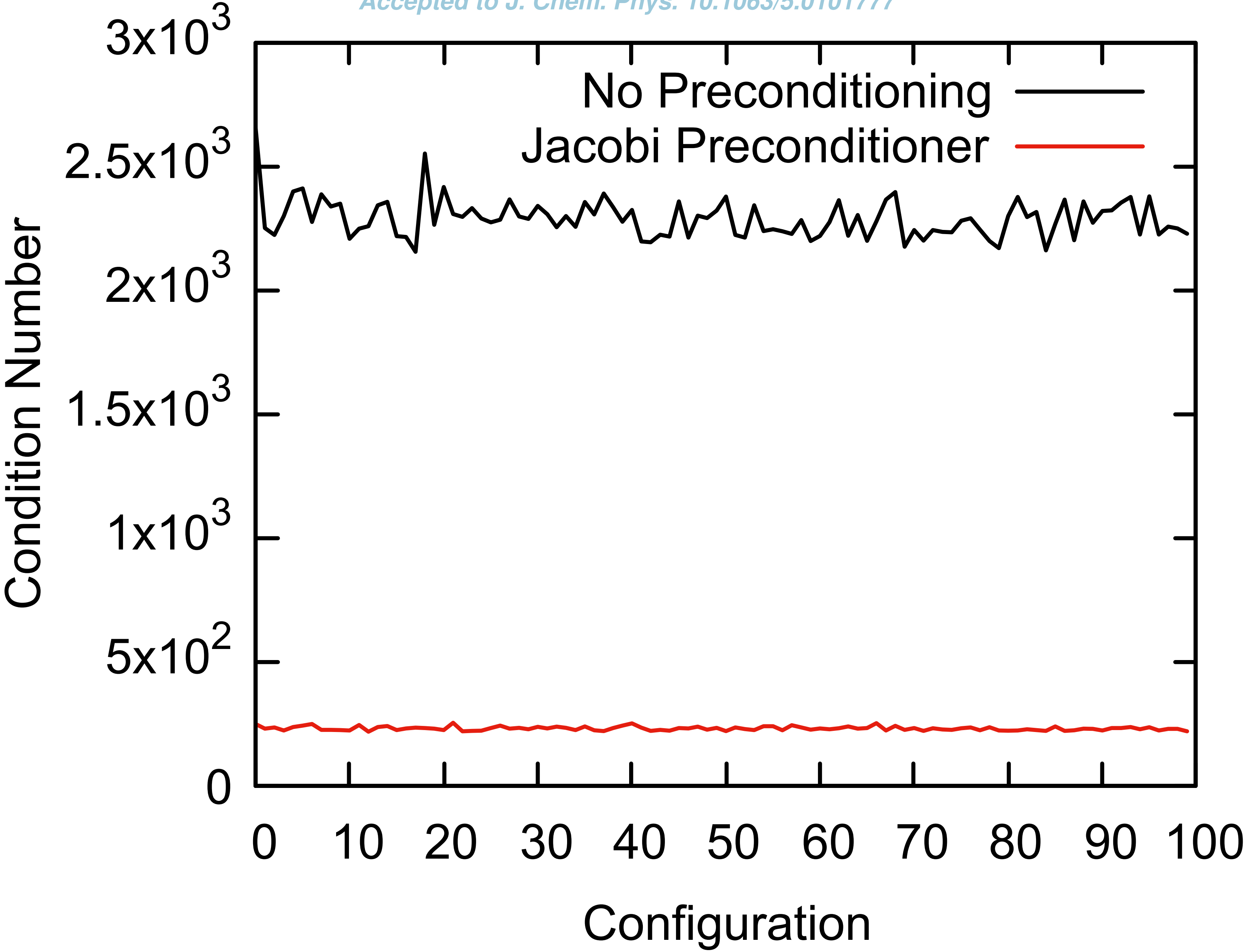

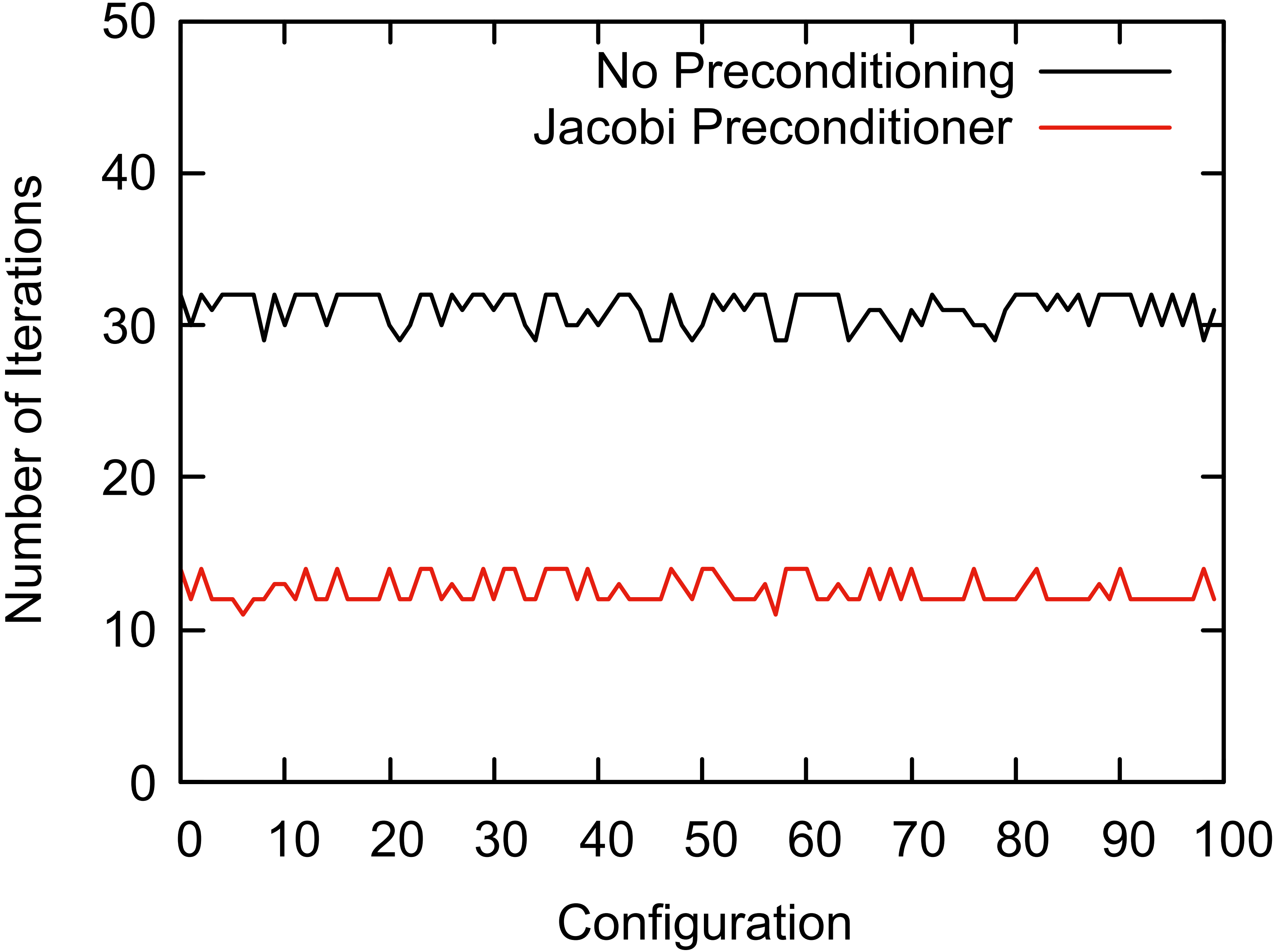
50
40
30
20
10
0
Number of Iterations
0
10
20
30
40
50
60
70
80
90
100
Configuration
No Preconditioning
Jacobi Preconditioner

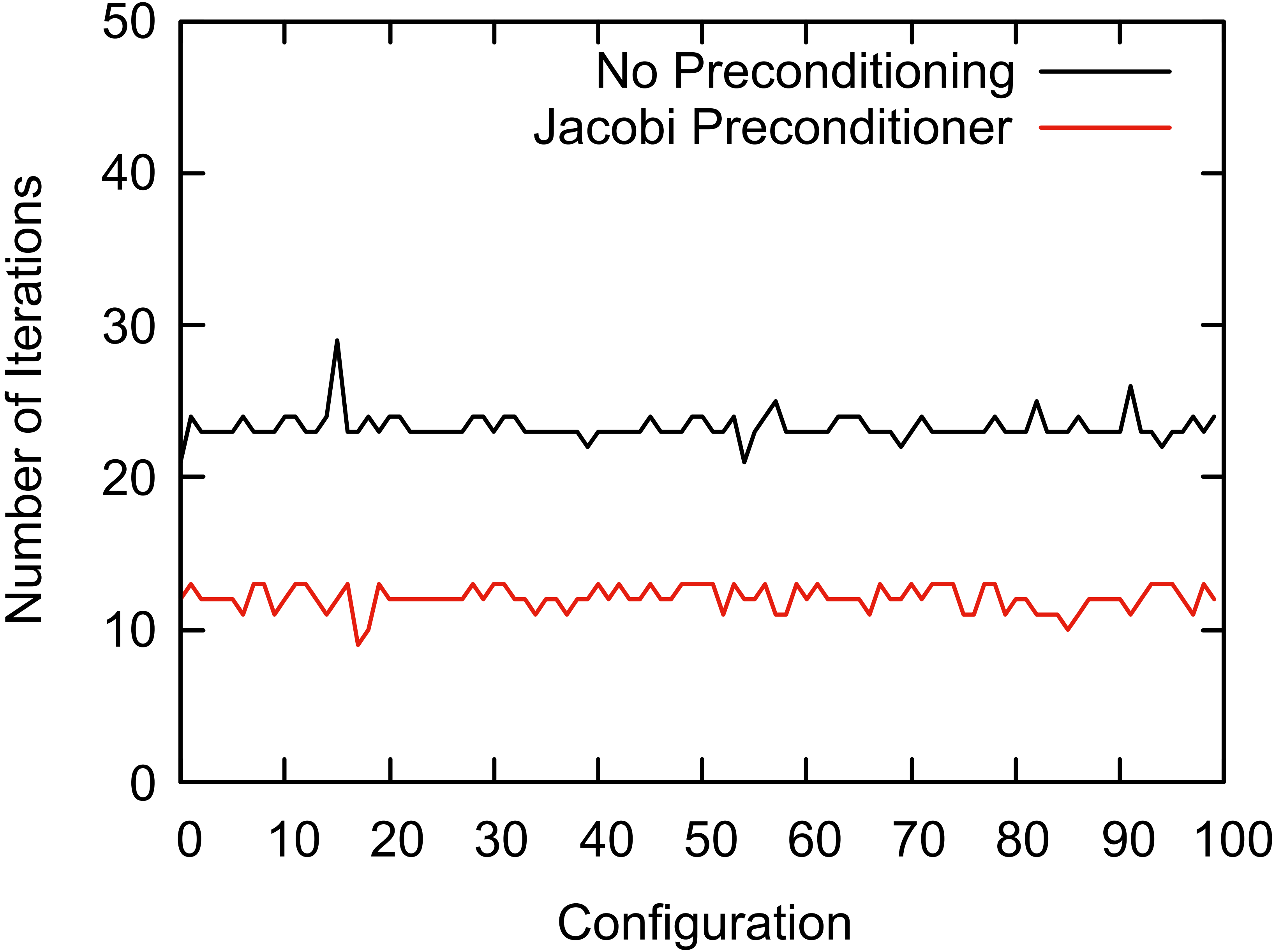
50
40
30
20
10
0
Number of Iterations
0
10
20
30
40
50
60
70
80
90
100
Configuration
No Preconditioning
Jacobi Preconditioner

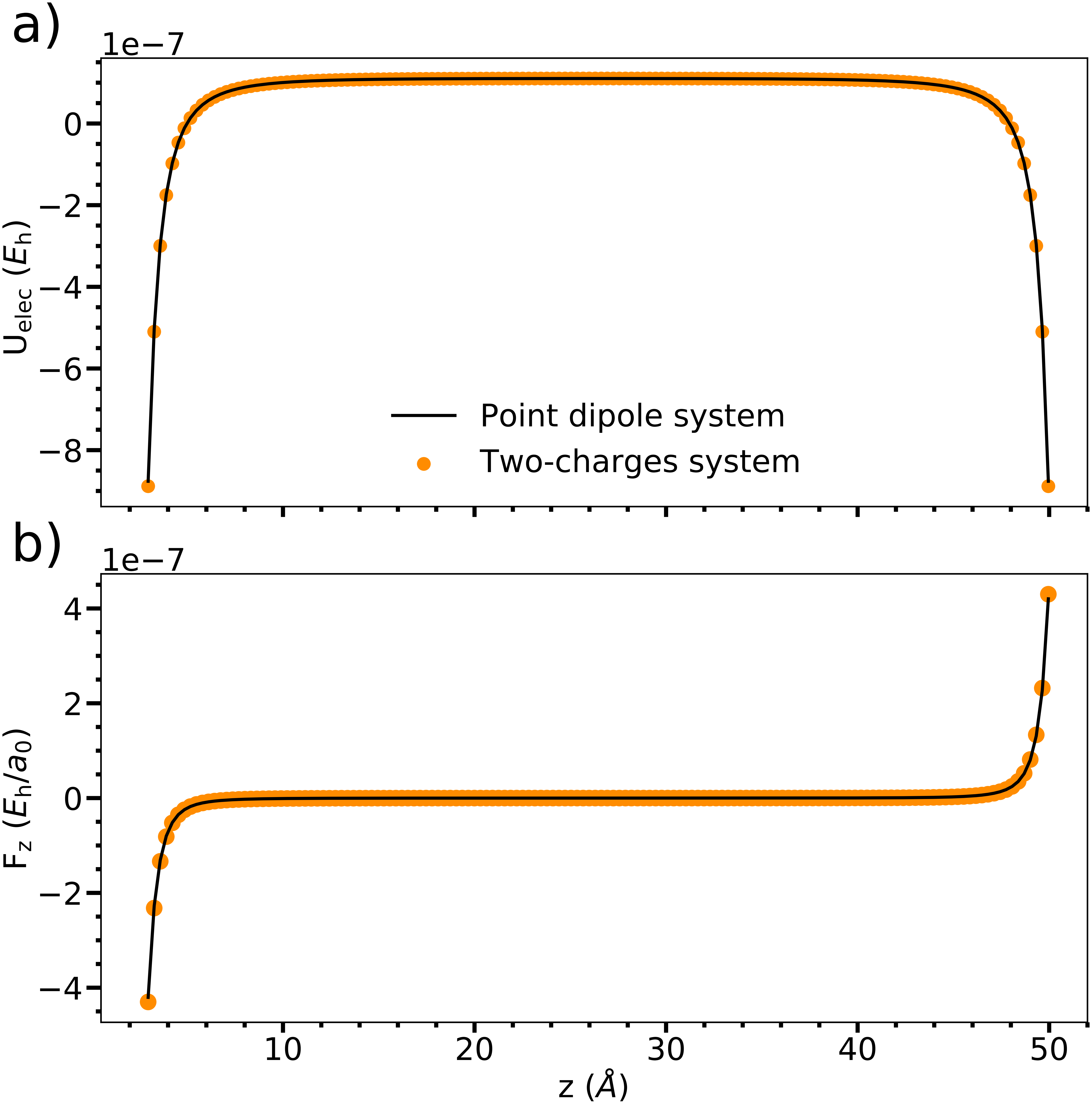
a)
1e−7
0
−2
−4
−6
−8
U_{elec} (E_h)
Point dipole system
Two-charges system
b)
1e−7
4
2
0
−2
−4
F_z (E_h/a_0)
10
20
30
40
50
z (Å)

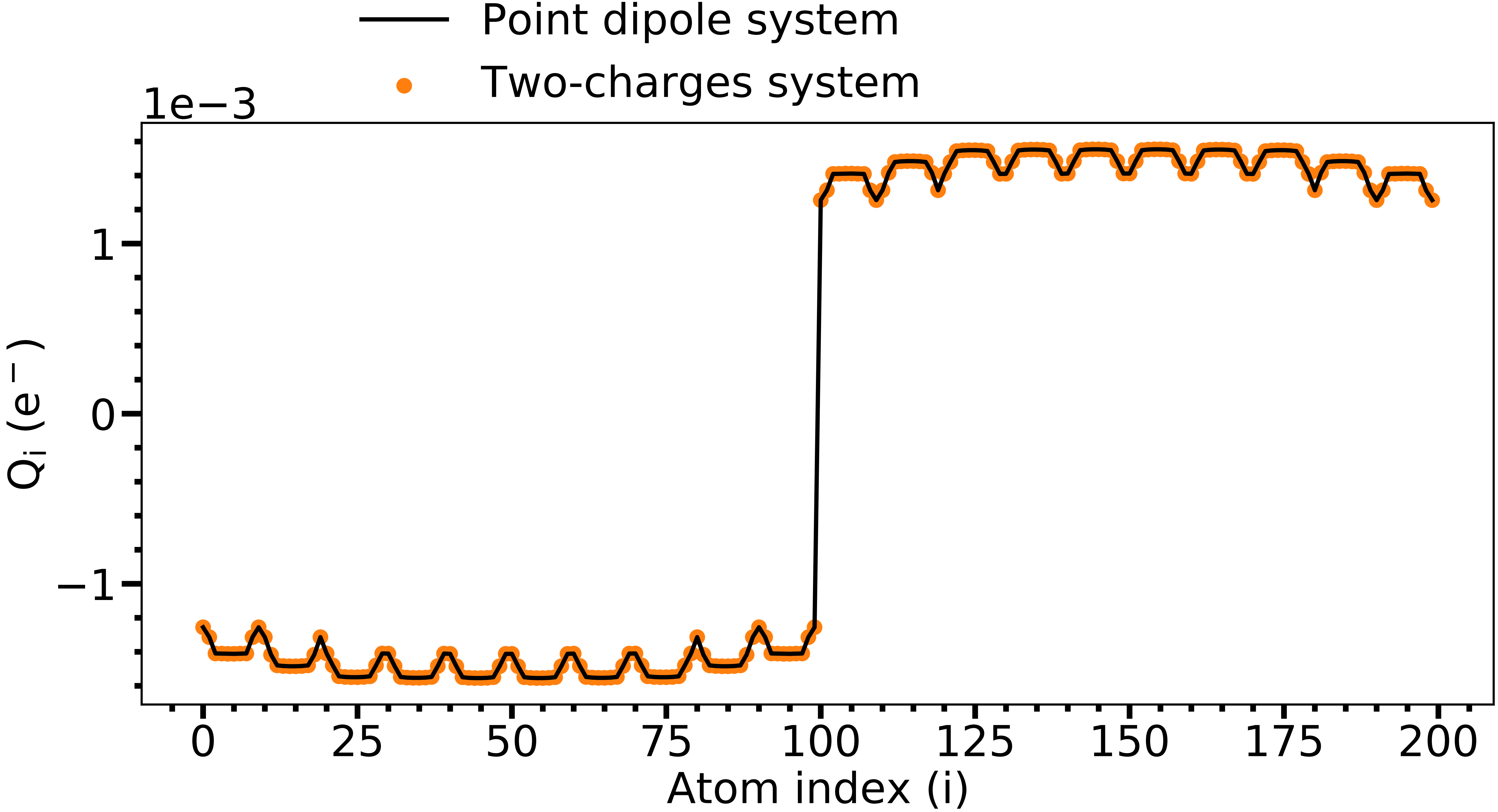
Point dipole system
Two-charges system
1e−3
1
0
−1
Q_i (e^-)
0
25
50
75
100
125
150
175
200
Atom index (i)

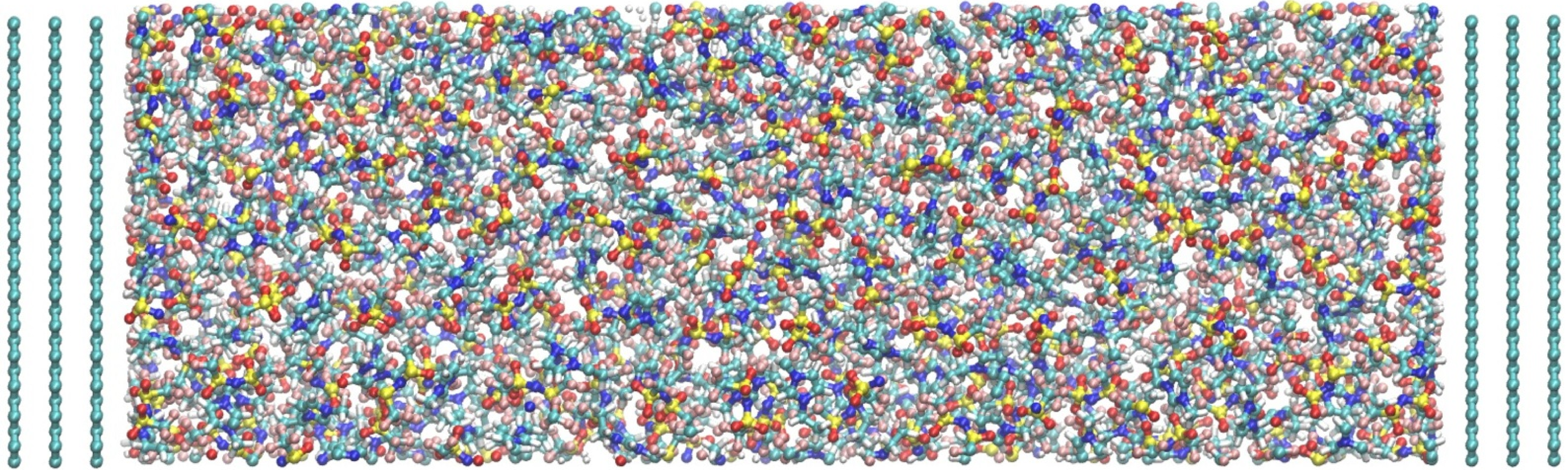

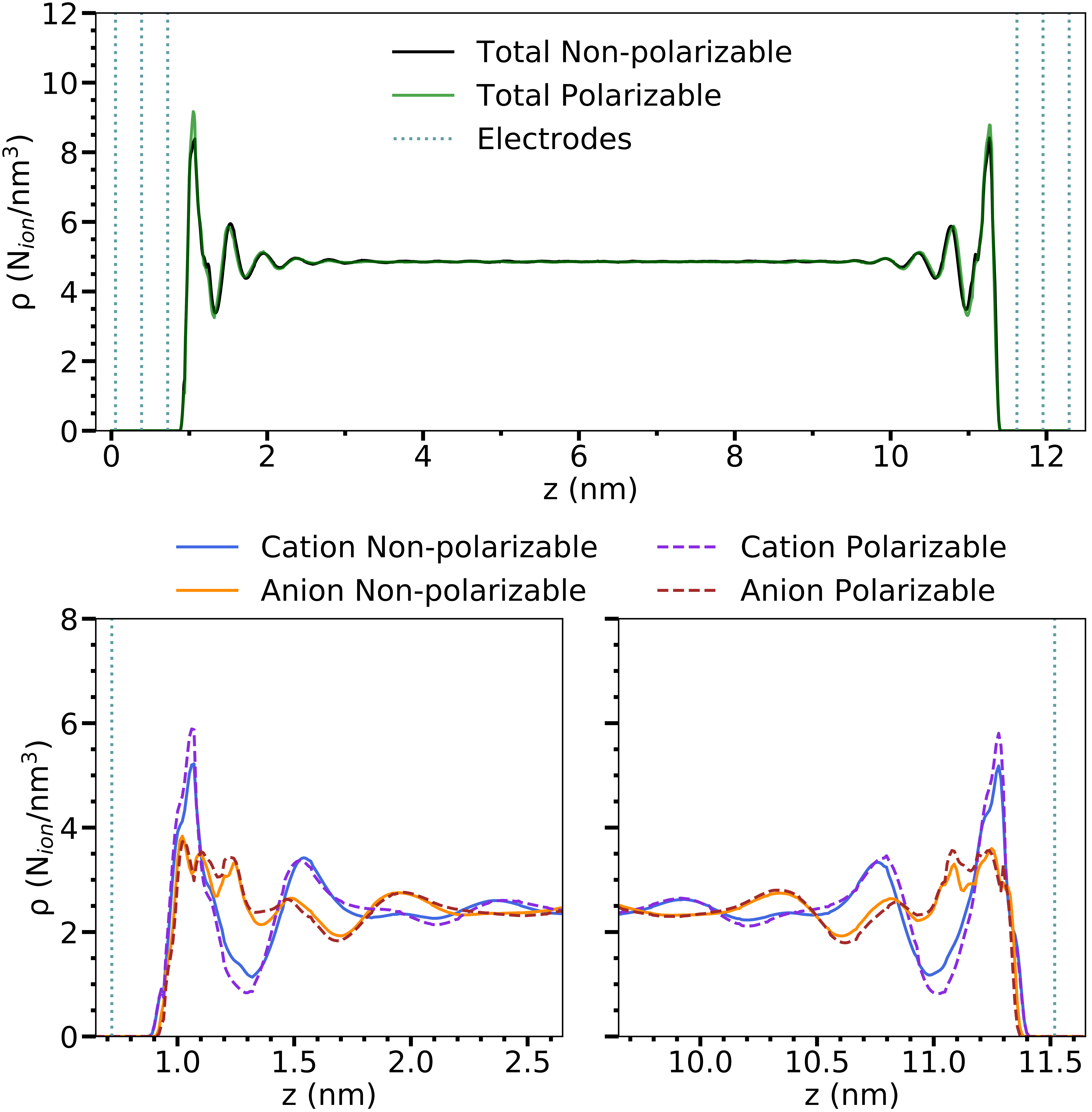
Total Non-polarizable
Total Polarizable
Electrodes
ρ (N_{ion}/nm^3)
z (nm)
0
2
4
6
8
10
12
Cation Non-polarizable
Anion Non-polarizable
Cation Polarizable
Anion Polarizable
1.0
1.5
2.0
2.5
10.0
10.5
11.0
11.5

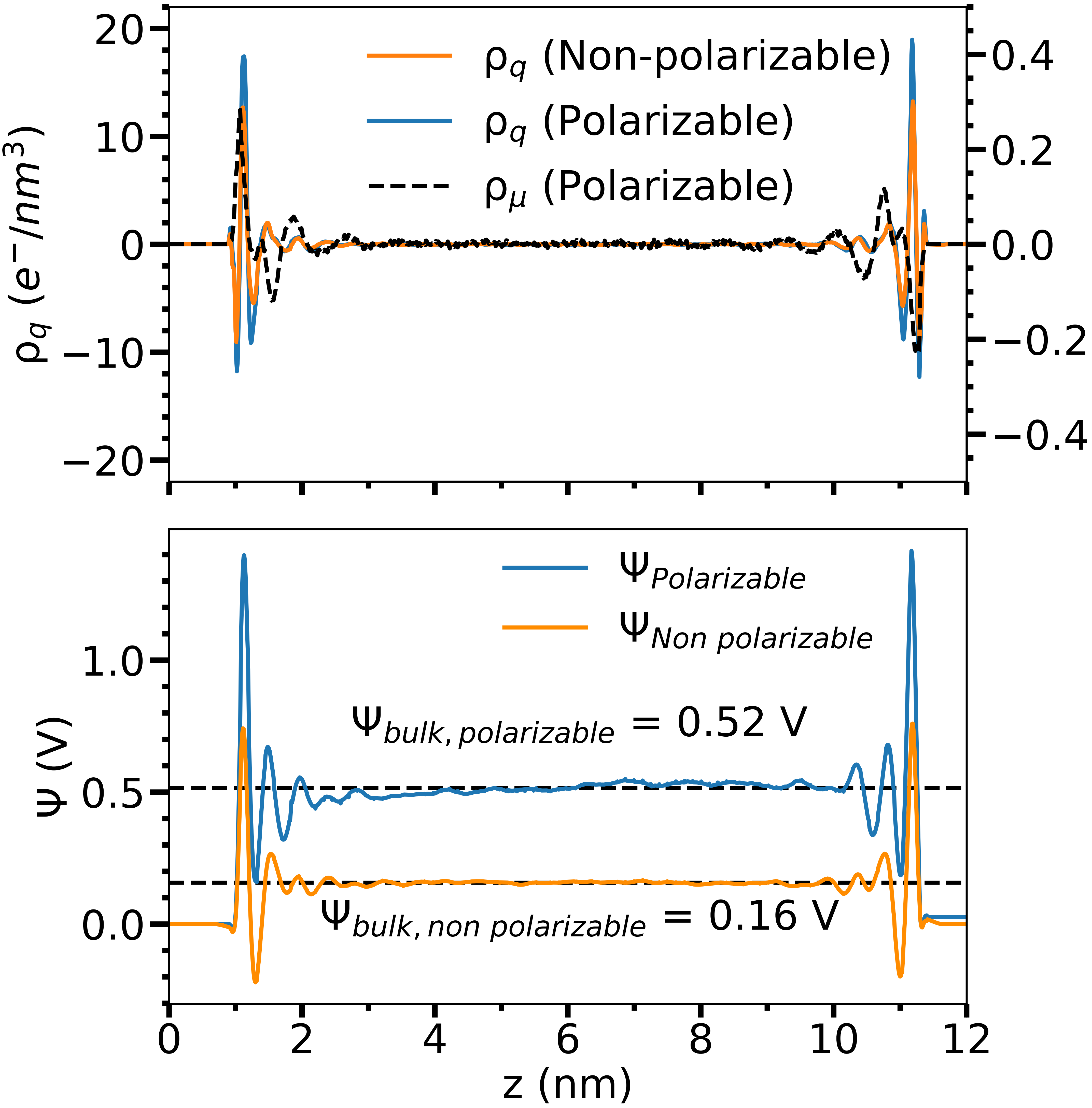
ρ_q (Non-polarizable)
ρ_q (Polarizable)
ρ_μ (Polarizable)
ρ_q (e⁻/nm³)
ρ_μ (e⁻/nm²)
20
10
0
−10
−20
0.4
0.2
0.0
−0.2
−0.4
Ψ_Polarizable
Ψ_Non polarizable
Ψ_bulk, polarizable = 0.52 V
Ψ_bulk, non polarizable = 0.16 V
Ψ (V)
1.0
0.5
0.0
0
2
4
6
8
10
12
z (nm)

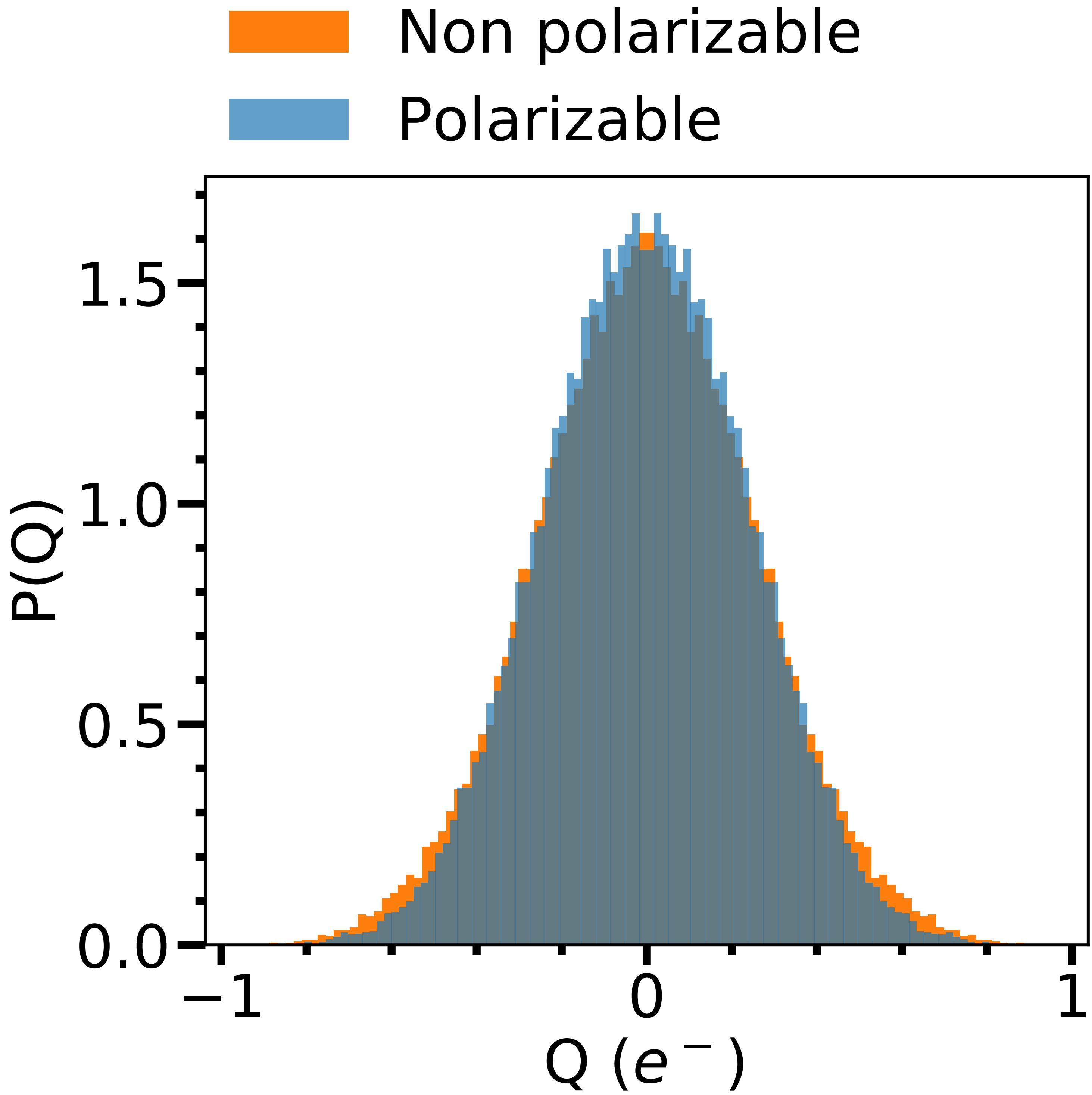
Non polarizable
Polarizable
P(Q)
1.5
1.0
0.5
0.0
−1
0
1
Q (e^-)

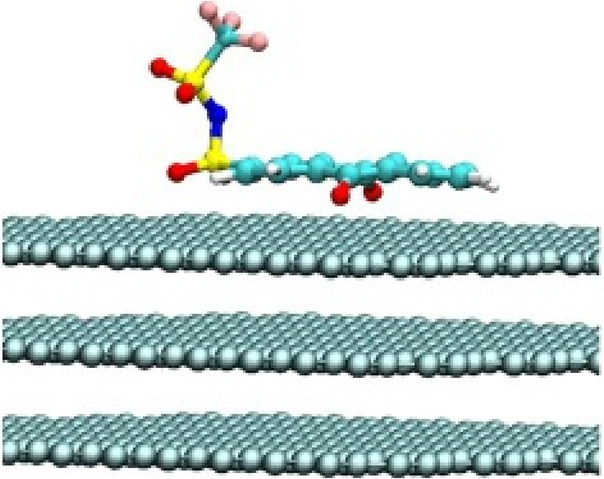

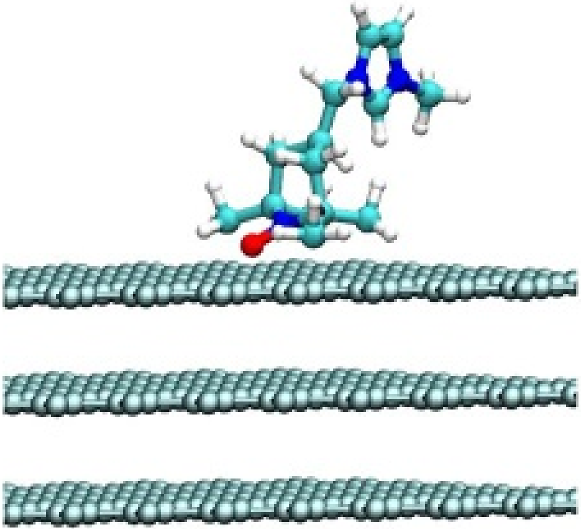

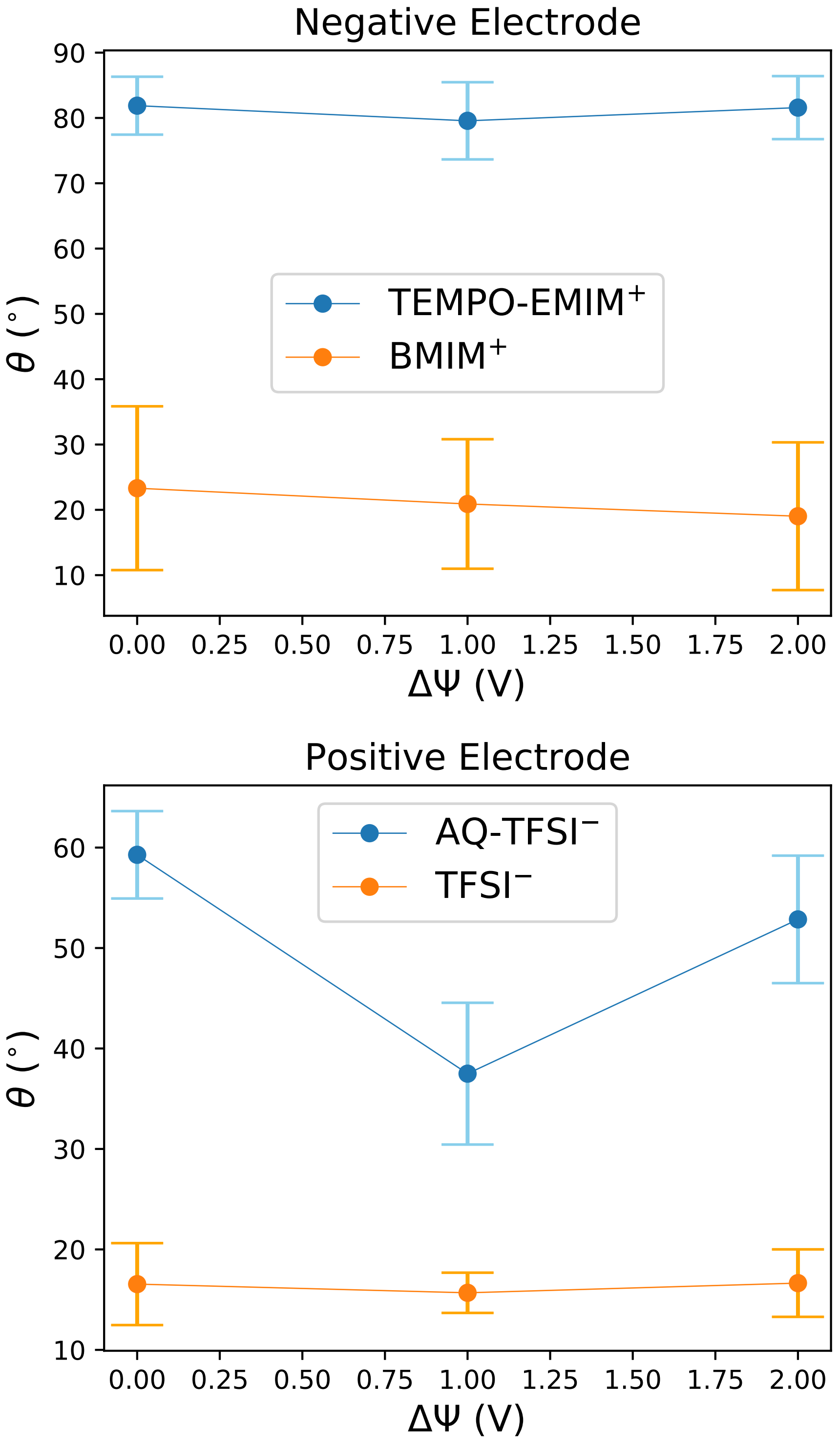
Negative Electrode
θ (°)
90
80
70
60
50
40
30
20
10
0.00
0.25
0.50
0.75
1.00
1.25
1.50
1.75
2.00
ΔΨ (V)
TEMPO-EMIM$^+$
BMIM$^+$
Positive Electrode
θ (°)
60
50
40
30
20
10
0.00
0.25
0.50
0.75
1.00
1.25
1.50
1.75
2.00
ΔΨ (V)
AQ-TFSI$^-$
TFSI$^-$